TRANSPORTED SNAPSHOT MODEL ORDER REDUCTION APPROACH FOR PARAMETRIC, STEADY-STATE FLUID FLOWS CONTAINING PARAMETER DEPENDENT SHOCKS

BY

NIRMAL JAYAPRASAD NAIR

THESIS

Submitted in partial fulfillment of the requirements
for the degree of Master of Science in Aerospace Engineering
in the Graduate College of the
University of Illinois at Urbana-Champaign, 2018

Urbana, Illinois

Adviser:

Assistant Professor Maciej Balajewicz

Abstract

In this thesis, a new model order reduction approach is proposed for parametric steady-state nonlinear fluid flows characterized by shocks and discontinuities whose spatial locations and orientations are strongly parameter dependent. In this method, solutions in the predictive regime are approximated using a linear superposition of parameter-dependent basis. The sought after parametric reduced-basis arise from solutions of linear transport equations. Key to the proposed approach is the observation that the optimal transport velocities are typically smooth and continuous, despite the solution themselves not being so. As a result, the transport fields can be accurately expressed using a low-order polynomial expansion. Similar to traditional projection-based model order reduction approaches, the proposed method is formulated mathematically as a residual minimization problem for the generalized coordinates. The method is successfully applied to the reduction of a parametric 1-D flow in a converging-diverging nozzle, a parametric 2-D supersonic flow over a forward facing step and a parametric 2-D jet diffusion flame in a combustor.

To my parents.

Acknowledgements

I would first like to thank my thesis adviser, Prof. Maciej Balajewicz, for his immense support and guidance throughout the tenure of this thesis. I am extremely grateful to him for providing the freedom to explore and implement new ideas but most importantly, for always keeping his doors open whenever I ran into trouble. Ranging from learning to do valuable research to improving my effective paper writing and presentation skills, he has helped me grow as a researcher. I would also like to thank my fellow lab-mates Rambod Mojgani and Francisco Gonzalez for the discussions I had with them which have indirectly played an important role in the development of my thesis. Finally, I would like to thank my parents and sister for their continuous love and support all the way from my home country.

Table of Contents

List of Figures

List of Tables

Chapter 1

Introduction

1.1 Motivation

Computational models of high-dimensional systems arise in a rich variety of engineering and scientific contexts. Computational Fluid Dynamics (CFD) for example has become an indispensable tool for many engineering applications across a wide range of industries. Unfortunately, high-fidelity CFD simulations are often so computationally prohibitive that they cannot be used as often as needed, or used only in special circumstances rather than routinely. Consequently, the impact of CFD on parametric and time-critical applications such as design, optimization, and control has not yet been fully realized. Model Order Reduction (MOR) is a serious contender for bridging this gap.

1.1.1 Existing MOR techniques

MOR is a family of techniques for reducing the computational complexity of large-scale high-fidelity models by generating low-dimensional, reduced-order models (ROMs). Most existing MOR approaches are based on projection. In projection-based MOR, the state variables are approximated in a low-dimensional subspace. In a purely data-driven context, the reduced-order basis (ROB) arise from some factorization of a snapshot matrix. A solution snapshot matrix is a matrix whose columns contains solutions of the high-fidelity model sampled at various times or parameters. Two popular approaches for identifying ROBs from snapshots include the proper orthogonal decomposition (POD) [1, 2] and dynamic mode decomposition (DMD) [3, 4]. The POD modes correspond to the left singular vectors of the snapshot matrix while DMD modes correspond to the eigenvectors of an empirically identified linear evolution operator acting on the snapshots. In the reduced-basis method [5, 6], snapshots are generated adaptively based on a greedy approach. It is possible to improve ROM accuracy by including some information about the dynamics of the system during the construction of the ROBs. For example, in balanced truncation [7, 8, 9], low combined observability and controllability measures are used to guide the reduction. Although usually more accurate than POD and DMD, balanced truncation requires solutions of Lyapunov equations and thus, is usually not tractable for

large-scale systems. In response, various approximate balanced techniques, including low-rank methods for Lyapunov equations [10, 11], balanced POD (BPOD) [12, 13], have been developed.

1.1.2   Parametric MOR

For a ROM to be truly useful, it must be capable of generating accurate predictions for parameter values that are different from those sampled for the purpose of constructing a ROB. Generating ROBs and ROMs that are robust to parameter variations is an active area of research [14]. The choice of parameter sample points is critical to any method used to generate the basis. For problems with small number of parameters, a simple approach like random sampling using the Latin hypercube method is often sufficient [15]. For problems with large number of parameters, more sophisticated sampling methods are usually required. In the standard greedy sampling approach [16, 17, 18, 19], the sample points are chosen one-by-one in an adaptive matter. At every iteration, the goal is to find the parameter value for which the error between the ROM and the full order model (FOM) is largest. The FOM is sampled at this point and the new information is used to generate a new reduced-basis.

Another critical issue involves the choice between a global or local basis. Global basis approximates a solution for any parameter in the parameter space and has been shown to perform adequately for many applications such as non-linear dynamical systems [20], fluid-structure modeling of an aircraft [21], CFD based aeroelastic computations [22], turbulent flows [23] and nozzle shape optimization [24]. But particularly challenging problems often necessitate the use of multiple local reduced basis [25, 26, 27]. In these cases, several local basis are constructed and linked to particular regions in the parameter or state space. During the evaluation of the solutions in the predictive regime, either these local basis or the ROM matrices are interpolated [28, 29] or the appropriate local basis is used depending on where the current high-fidelity solution lies [30, 31]. The price of this additional flexibility are the switching algorithms required to switch between the local basis.

1.1.3   Parametric MOR for fluid flows containing parameter dependent shocks

Achieving parametric robustness is particularly challenging when the sought after solutions contain parameter dependent shocks, sharp gradients or discontinuities. These situations arise in a wide range of important engineering applications, for example, high-speed fluid flows [32, 33], multi-phase flows with evolving material interfaces [34], computational finance [35] and structural contact problem with evolving contact regions [36]. POD modes of flow snapshots containing evolving discontinuities and shocks in parameter space show slow decay of singular values. Hence, above-mentioned MOR techniques would fail to provide

accurate predictions for these types of solutions in the predictive regime.

Over the years, a large variety of discontinuity-aware MOR techniques have been developed. In the first class of such methods, the problem of modeling discontinuities is avoided entirely by exploiting symmetry and transport reversal properties of certain hyperbolic PDEs [37, 38, 39]. These methods identify a symmetry-reduced structure or template of the solution from the snapshot matrix which is then subjected to various transport operations to predict new solutions. A variation of this technique involves linear decomposition of the solution into global and advection modes governed by optimal mass transfer [40] where the global modes characterize diffusion whereas advection modes capture transport properties. In L_1-dictionary approach [41] the solution is given by a linear combination of local dictionary elements and L_1-norm of the residual is minimized.

More direct modeling of discontinuities includes basis splitting [42] or decomposing the solution into a variable separable form consisting of an evolution term to capture moving shocks and a diffusion term to capture the changing shapes [43]. For unsteady solutions with shocks, accurate low-rank solutions can be obtained using a Lagrangian framework [44] where both position and state of Lagrangian particle variables are approximated by their respective ROBs. Other methods avoid the problem of modeling discontinuities by domain decomposition where direct numerical simulation or reconstruction methods are used in regions containing the discontinuities [45, 46, 47].

Recently, a new class of parametric MOR based on, but not limited to, snapshot transformation is gaining popularity. This class of methods involve modification of the snapshot matrix such that the modified snapshots can be used to construct a low-dimensional subspace. For unsteady problems, the modified snapshots are evaluated by transformation of the physical domain based on known unsteady transport phenomena [48]. POD analysis of such a modified snapshot matrix would display quick decay of singular values enabling it to be used along with traditional MOR techniques. In the case of steady flow problems, the transport phenomena can be identified by training the snapshot data. Interpolation of modified snapshots based on these transports provides an approximate predictive solution [49].

1.2   Thesis contribution and outline

1.2.1   Contributions

The main aim of this thesis is to present a novel model order reduction approach capable of accurately predicting steady flow solutions characterized by parameter dependent shocks and discontinuities.

Our proposed approach shares similarities with previous parametric MOR techniques in the literature.

3

Similar to Iollo and Lombardi [40], and Welper [49], we approximate the sought after solutions as a superposition of transformed, precomputed snapshots. However, in contrast to these previous approaches, our proposed approach is projection-based. One of the potential advantages of projection-based methods is that they retain the underlying structure of the dynamical system and thus provide, in principle, more robust predictive capabilities. Finally, similar to Abgrall et al. [41], we minimize the system residual in the ℓ_1 norm which has been shown to be beneficial for problems containing shocks and discontinuities.

1.2.2   Outline

The thesis is organized as follows. In Chapter 2, the problem of interest is defined and traditional projection-based model order reduction is recapitulated. In Chapter 3, the proposed new approach – hereafter referred to as transported snapshot model order reduction approach (TSMOR) – is introduced. In Chapter 4, TSMOR is integrated with a hyper-reduction algorithm. In Chapter 5, the performance of the proposed method is evaluated on several representative 1D and 2D fluid flow problems. Finally, in Chapter 6, the contributions of the thesis and prospects for future work are summarized.

Chapter 2

Traditional model order reduction techniques

2.1 Full order model

We consider large-scale computational models arising from semi-discretization of hyperbolic or convection-dominated parabolic PDEs such as the Euler or high-Reynolds-number Navier-Stokes equations:

$$\frac{d\boldsymbol{w}(t;\boldsymbol{\mu})}{dt} + f(\boldsymbol{w}(t;\boldsymbol{\mu}), t; \boldsymbol{\mu}) = \boldsymbol{0} \tag{2.1}$$

with suitable initial data $\boldsymbol{w}(0;\boldsymbol{\mu}) = \boldsymbol{w}_0(\boldsymbol{\mu})$ and boundary conditions. Here $t \in [0, t_{\max}]$ denotes time, $\boldsymbol{w}(t;\boldsymbol{\mu}) \in \mathbb{R}^{N_w}$ denotes a vector of N_w high dimensional state variables, $\boldsymbol{\mu} \in \mathcal{D} \subset \mathbb{R}^{N_d}$ (where $\mathcal{D}$ is a bounded domain) is a vector of N_d parameters, and $\boldsymbol{f} : \mathbb{R}^{N_w} \times [0, t_{\max}] \times \mathcal{D} \to \mathbb{R}^{N_w}$ are nonlinear functions approximating the convective and diffusive fluxes. The steady state equation for this system can be written as:

$$R\left(\boldsymbol{w}(\boldsymbol{\mu}); \boldsymbol{\mu}\right) \coloneqq f(\boldsymbol{w}(\boldsymbol{\mu}); \boldsymbol{\mu}) = \boldsymbol{0} \tag{2.2}$$

where $R(\boldsymbol{w}(\mu); \mu)$ is the steady state residual. To obtain steady state solutions, Eq. (2.2) can be solved directly by an iterative method or a time-stepping method can be used to advance the unsteady Eq. (2.1) to a steady state solution. We refer to Eq. (2.1) as the full order model (FOM).

2.2 ==Dimensionality reduction==

In traditional projection-based MOR, the state vector $\boldsymbol{w}(\boldsymbol{\mu}) \in \mathbb{R}^{N_w}$ is approximated in a trial subspace as follows

$$\boldsymbol{w}(\boldsymbol{\mu}) \approx \boldsymbol{w}_r(\boldsymbol{\mu}) = \boldsymbol{U}\boldsymbol{a}(\boldsymbol{\mu}) \tag{2.3}$$

where $\boldsymbol{U} \in \mathbb{R}^{N_w \times N_k}$ is a matrix whose columns contain the basis of this subspace, $N_k \ll N_w$ is the reduced dimension, and $\boldsymbol{a}(\boldsymbol{\mu}) \in \mathbb{R}^{N_k}$ denotes the generalized coordinates in this basis. Substituting the approximation (2.3) into the residual equation (2.2) yields $R\left(\boldsymbol{U}\boldsymbol{a}(\boldsymbol{\mu}); \boldsymbol{\mu}\right) = \boldsymbol{0}$, which represents an overdetermined system of

N_w equations and N_k unknowns. Consequently, the vector of generalized coordinates is chosen to minimize the residual

$$\min_{\boldsymbol{a}} \| R\left(\boldsymbol{U}\boldsymbol{a}(\boldsymbol{\mu}); \boldsymbol{\mu}\right) \|_p \tag{2.4}$$

where $\|\cdot\|_p$ is the standard ℓ_p-norm. We refer to Eq. (2.4) as the reduced-order model (ROM).

In the case of the ℓ_2-norm, the nonlinear system of equations can be solved iteratively using, for example, the Gauss-Newton method, which can be summarized as *for $i = 1, \ldots, r$ solve*

$$\min_{\boldsymbol{\Delta}\boldsymbol{a}^{(i)}} \| \boldsymbol{J}^{(i)}\boldsymbol{U}\boldsymbol{\Delta}\boldsymbol{a}^{(i)} + R(\boldsymbol{U}\boldsymbol{a}^{(i)}; \boldsymbol{\mu}) \|_2 \tag{2.5}$$

where the superscript (i) designates the i-th iteration, $\boldsymbol{\Delta}\boldsymbol{a}^{(i)}$ is the increment of the sought-after solution at the i-th Gauss-Newton iteration, and r is determined by a convergence criterion.

Eq. (2.5) constitutes a k-dimensional Gauss-Newton ROM of FOM. The normal equations associated with Eq. (2.5) can be written as

$$(\boldsymbol{J}^{(i)}\boldsymbol{U})^T \boldsymbol{J}^{(i)}\boldsymbol{U}\boldsymbol{\Delta}\boldsymbol{a}^{(i)} = -(\boldsymbol{J}^{(i)}\boldsymbol{U})^T R(\boldsymbol{U}\boldsymbol{a}^{(i)}) \tag{2.6}$$

This minimization can be shown to be equivalent to a Petrov–Galerkin projection of the residual equation (2.2) with test subspace $\boldsymbol{\Phi} = \boldsymbol{J}\boldsymbol{U}$. For nonlinear, non-self adjoining problems, this approach is more robust than a Galerkin projection $\boldsymbol{\Phi} = \boldsymbol{U}$.

2.3 Computation of basis

In data-driven projection-based MOR, the ROBs are usually constructed offline by collecting solution snapshots of problem (2.2) for different instances of the parameters $\boldsymbol{\mu}$. Specifically, for each sampled parameter vector $\boldsymbol{\mu}_s$, $s = 1, \cdots, N_s$, the computed snapshots are gathered in a matrix $\boldsymbol{M}$, with $M_{(:,s)} := \boldsymbol{w}(\boldsymbol{\mu}_s)$ where the notation $(:, s)$ denotes the sth column vector of the matrix. For the sake of brevity, only the POD approach is considered in this section to motivate the construction of global and local ROBs. The results presented here however, are general and thus, applicable to most other popular ROB generation strategies.

2.3.1 Global basis

In this approach, the trial basis is global in the sense that a single matrix $\boldsymbol{U}$ is used to approximate the solution $\boldsymbol{w}(\boldsymbol{\mu})$ in the entire parameter space $\mathcal{D}$. Global POD basis are obtained by evaluating the singular

value decomposition (SVD) of the snapshot matrix $\boldsymbol{M}$:

$$\boldsymbol{M} = \boldsymbol{U}\boldsymbol{\Sigma}\boldsymbol{V}^T \tag{2.7}$$

where $\boldsymbol{U} \in \mathbb{R}^{N_w \times N_s}$ and $\boldsymbol{V} \in \mathbb{R}^{N_s \times N_s}$ are the left and right singular vectors of $\boldsymbol{M}$, respectively. $\boldsymbol{\Sigma} \in \mathbb{R}^{N_s \times N_s}$ is a diagonal matrix containing the singular values of $\boldsymbol{M}$ in descending order. POD basis is then constructed by choosing the first k columns of $\boldsymbol{U}$ which correspond to the k largest singular values. The POD basis is optimal in the sense that, for an orthonormal basis of size k, it minimizes the least-squares error between the original and reconstructed snapshot matrix,

$$\min_{\boldsymbol{U} \in \mathbb{R}^{N_w \times k}} \|\boldsymbol{M} - \boldsymbol{U}\boldsymbol{U}^T\boldsymbol{M}\|_2^2 \tag{2.8}$$

The global basis approach provides several benefits, for instance, evaluation of global basis is computationally straightforward and cheap because it involves only a one-time evaluation of a single matrix $\boldsymbol{U}$ which can be used to approximate a solution at any new parameter. Unfortunately, this approach is prone to low robustness toward problems with large parameter variations. Furthermore, the singular values show slow decay for flow problems containing parameter dependent shocks and discontinuities, limiting the efficient truncation of POD basis.

2.3.2 Local basis

To mitigate the above-mentioned issues concerning the global basis approach, it is preferable to approximate the solution $\boldsymbol{w}(\boldsymbol{\mu})$ using a set of local basis [31]. In the offline stage of this approach, N_s snapshots in $\boldsymbol{M}$ are clustered into N_v groups according to the relative distance between the snapshots. The optimal metric for measuring this distance is problem specific. It may be based on the values of the states, output of interest or, more relevant to this thesis, the distance between the parameters associated with the snapshots. For instance, all the snapshots corresponding to the parameters lying in a parameter sub-domain $\mathcal{D}_i \subset \mathcal{D}$, are grouped together in a matrix $\boldsymbol{M}_i$. Then local basis $\boldsymbol{U}_i$ for $i = 1, 2, \cdots, N_v$ are generated and assigned to each sub-domain in the solution space. The local basis are constructed either by computing the singular value decomposition of $\boldsymbol{M}_i$,

$$\boldsymbol{M}_i = \boldsymbol{U}_i\boldsymbol{\Sigma}_i\boldsymbol{V}_i^T \tag{2.9}$$

and truncating $\boldsymbol{U}_i$ to the first k_i columns [31] or by setting the local basis to be equal to the local snapshot matrix in the respective sub-domain, i.e. $\boldsymbol{U}_i = \boldsymbol{M}_i$ [41].

Then, in the online stage, the appropriate sub-domain $\mathcal{D}_i$ for $\boldsymbol{\mu}$ is identified and the associated local basis $\boldsymbol{U}_i$ are used to approximate the solution.

2.4 Drawbacks of traditional MOR techniques

For a ROM to be useful, it must be capable of providing solutions at parameters $\boldsymbol{\mu}^*$ not sampled during the offline basis construction phase, $\boldsymbol{\mu}^* \neq \boldsymbol{\mu}_s$. Although parameter robustness is an active area of research, it is particularly challenging when the sought after solutions contain discontinuities or sharp gradients whose spatial orientations are strongly parameter dependent. To illustrate, consider the toy problem of approximating the function $w(x) = H(x)$, $x = [-1, 1]$ using N_k global basis functions $u_i(x) = H(x + \mu_i)$ where H is the Heaviside function and $\mu_i = -0.5 + (i - 1)/(N_k - 1)$ for $i = 1, \ldots, N_k$. Note that for all N_k, none of the reduced-basis u_i contain a discontinuity coincident with the sought after solution – this is typical in the type of problems considered in this manuscript. It is straightforward to show that the optimal prediction of $w(x)$ is simply $w_r = 1/2(u_{N_k/2} + u_{N_k/2+1})$. This toy problem demonstrates that: (a) optimal constructions of solutions characterized by parameter dependent shocks and discontinuities are typically local and sparse in the sense that only two basis were used for reconstruction, and (b) the optimal construction using traditional POD modes provides a "staircase" approximation of the true solution.

In summary, neither global nor local reduced-basis can be expected to yield efficient approximations in the predictive regime of solutions characterized by shocks, discontinuities, and sharp gradients whose physical locations and orientations are parameter dependent. Unfortunately, these conditions are rarely satisfied in practice.

Chapter 3

Transported Snapshot Model Order Reduction (TSMOR)

3.1 Methodology

In this chapter, we introduce and summarize our new MOR approach for parametric and steady nonlinear fluid flows characterized by moving shocks, discontinuities and sharp gradients. In this proposed new approach, solutions at an unsampled parameter $\boldsymbol{\mu}^* \neq \boldsymbol{\mu}_s$ are approximated using a local and parameter-dependent trial subspace. Thus, if $\boldsymbol{w}(\boldsymbol{\mu}_{k_n})$ for $n = 1, \cdots, N_k$ where $\boldsymbol{\mu}_{k_n} \in \boldsymbol{\mu}_s$ is a subset of the solution snapshots computed offline, the solution at the new parameter is approximated by

$$\boldsymbol{w}(\boldsymbol{\mu}^*) \approx \boldsymbol{w}_r(\boldsymbol{\mu}^*) = \boldsymbol{U}(\boldsymbol{\mu}^*)\boldsymbol{a}(\boldsymbol{\mu}^*) \tag{3.1}$$

where $\boldsymbol{U}(\boldsymbol{\mu}^*) \in \mathbb{R}^{N_w \times N_k}$ is a matrix whose columns contain the *transported* solution snapshots $\boldsymbol{w}'(\boldsymbol{\mu}_{k_n}, \boldsymbol{\mu}^*)$ of the corresponding snapshots $\boldsymbol{w}(\boldsymbol{\mu}_{k_n})$.

A transported snapshot is here defined as a solution of a transport equation. More precisely, if $\boldsymbol{w}(\boldsymbol{\mu}_{k_n})$ is the vector of state variables on a computational grid with Cartesian coordinates $\boldsymbol{x}_i \in \mathbb{R}^{N_x}$ for $i = 1, 2, 3$, then in the Lagrangian frame of reference, the transported solution snapshot is given by:

$$\boldsymbol{x}_i'(\boldsymbol{\mu}_{k_n}, \boldsymbol{\mu}^*) = \boldsymbol{x}_i + \boldsymbol{\sigma}(\boldsymbol{\Delta\mu}), \quad \text{for } i = 1, 2, 3, \text{ and } n = 1, \dots, N_k \tag{3.2}$$

where the transport $\boldsymbol{\sigma}(\boldsymbol{\Delta\mu}) \in \mathbb{R}^{N_x}$, is a function of the parameter variation $\boldsymbol{\Delta\mu}$ defined as: $\boldsymbol{\Delta\mu} = (\boldsymbol{\mu}^* - \boldsymbol{\mu}_{k_n}) \oslash \boldsymbol{\Delta\mu}_d$ for $n = 1, ..., N_k$, where $\oslash$ denotes componentwise division. The reference vector $\boldsymbol{\Delta\mu}_d \in \mathbb{R}^{N_d}$ is used to normalize the magnitudes of the individual parameter variations. In this work, $\boldsymbol{\Delta\mu}_d$ is taken to be the size of the parameter sampling interval. Finally, the sought after transported snapshots $\boldsymbol{w}'(\boldsymbol{\mu}_{k_n}, \boldsymbol{\mu}^*)$ are evaluated by interpolating $\boldsymbol{w}(\boldsymbol{\mu}_{k_n})$ from $\boldsymbol{x}_i'$ back to the original Eulerian computational grid $\boldsymbol{x}_i$.

In principle, this new proposed transported snapshot approximation given by Eq. (3.1) can be incorporated

into a traditional, residual-based framework as follows:

$$\min_{\boldsymbol{\sigma},\boldsymbol{a}}\|R(\boldsymbol{U}(\boldsymbol{\mu^*})\boldsymbol{a}(\boldsymbol{\mu^*});\boldsymbol{\mu^*})\|_p \tag{3.3}$$

where $\boldsymbol{a}(\boldsymbol{\mu^*})$ are the generalized coordinates and $\boldsymbol{\sigma}(\boldsymbol{\Delta\mu})$ are the transport vectors. However clearly, such a naive implementation cannot be expected to be tractable in practice because the number of variables scales with the size of the original, high-fidelity FOM. Although techniques like hyper-reduction have been available for some time, these methods only alleviate the cost of the objective function evaluations, and not the number of the optimization variables. Additional layers of approximation are therefore required to efficiently implement the new proposed approach in a residual-based MOR framework.

Our first additional approximation is motivated by the observation that, for a large class of problems, the optimal transports are smooth functions of the parameter variations. In other words, the transports admit a low-order, multi-variate polynomial expansion in $\boldsymbol{\Delta\mu}$ as follows:

$$\boldsymbol{\sigma}(\boldsymbol{\Delta\mu}) \approx \boldsymbol{\sigma}_1(\boldsymbol{\mu}_{k_n})\Delta\mu_1 + \boldsymbol{\sigma}_2(\boldsymbol{\mu}_{k_n})\Delta\mu_2 + \ldots + \boldsymbol{\sigma}_{N_d+1}(\boldsymbol{\mu}_{k_n})\Delta\mu_1^2 + \boldsymbol{\sigma}_{N_d+2}(\boldsymbol{\mu}_{k_n})\Delta\mu_1\Delta\mu_2 + \ldots \tag{3.4}$$

where $\boldsymbol{\sigma}_j(\boldsymbol{\mu}_{k_n})$ for $j = 1,\ldots,N_l$ are the coefficients of the polynomial expansion. Eq. (3.4) can also be expressed in matrix form:

$$\boldsymbol{\sigma}(\boldsymbol{\Delta\mu}) = \boldsymbol{\Psi}(\boldsymbol{\mu}_{k_n})\boldsymbol{d}(\boldsymbol{\Delta\mu}) \tag{3.5}$$

where the columns of the matrix $\boldsymbol{\Psi}(\boldsymbol{\mu}_{k_n}) \in \mathbb{R}^{N_x \times N_l}$ contain the coefficients of polynomial expansion, i.e. $\boldsymbol{\Psi}(\boldsymbol{\mu}_{k_n})_{(:,j)} = \boldsymbol{\sigma}_j(\boldsymbol{\mu}_{k_n})$. The vector $\boldsymbol{d}(\boldsymbol{\Delta\mu}) \in \mathbb{R}^{N_l}$ contains the monomials constituting the variables of the polynomial expansion (3.4) given by:

$$d_j(\boldsymbol{\Delta\mu}) = \prod_{i=1}^{N_d} (\Delta\mu_i)^{f_{j,i}} \quad \text{for } f_{j,i} \in \mathbb{Z} \text{ and } j = 1,\ldots,N_l \tag{3.6}$$

Our second, and final additional approximation is motivated by the observation that $\boldsymbol{\sigma}(\boldsymbol{\Delta\mu})$ – in addition to being a smooth function of the parameter variations – is also smooth in space. Indeed, for the toy problem considered in Sec. 2.4, it can be shown that $\boldsymbol{\sigma}_j = p_j \mathbf{1}_{N_x \times 1}$ where each p_j is a scalar. As a consequence, we assume that each coefficient $\boldsymbol{\sigma}_j(\boldsymbol{\mu}_{k_n})$ in Eq. (3.4) admits its own, low-order expansions. More specifically, we assume that each coefficient $\boldsymbol{\sigma}_j(\boldsymbol{\mu}_{k_n})$ in (3.4) can be approximated using a Fourier series:

$$\boldsymbol{\sigma}_j(\boldsymbol{\mu}_{k_n}) = \sum_{p,q,r\in\mathbb{Z}} c_{p,q,r}^{s(j)} e^{ipx_1} e^{iqx_2} e^{irx_3} \quad \text{for } j = 1,\ldots,N_l \tag{3.7}$$

10

where m is the number of harmonics retained in the expansion and $\boldsymbol{c}^s := c_{p,q,r}^{s(j)}$ are the coefficients of the Fourier expansion.

These two additional approximations have the following two important consequences. First, since the optimal transport is assumed to be a polynomial function of the parameter variations, its coefficients can be precomputed, offline, once and for all. More specifically, given a snapshot matrix $\boldsymbol{M}$, the coefficient $\boldsymbol{\sigma}_j(\boldsymbol{\mu}_{k_n})$ in (3.4) can be identified using a standard least-squares fitting procedure (refer to Sec. 3.2 for more details). Moreover, because each coefficient is approximated by a low order Fourier series expansion, the offline fitting procedure only requires the identification of the relatively small number of coefficients of the Fourier expansion. The second and final important consequence of these two additional assumptions is that now, the online residual minimization problem is only a function of the generalized coordinates:

$$\min_{\boldsymbol{a}} \| R(\boldsymbol{U}(\boldsymbol{\mu}^*)\boldsymbol{a}(\boldsymbol{\mu}^*); \boldsymbol{\mu}^*) \|_p \tag{3.8}$$

and thus, standard hyper-reduction techniques can be applied to alleviate the cost of objective function evaluations.

In summary, our proposed new approach can be decomposed into the standard offline-online strategy:

1. Offline stage: In this stage, the FOM is sampled in the parameter domain and the solutions are stored in a snapshot matrix $\boldsymbol{M}$. The optimal transport matrix $\boldsymbol{\Psi}(\boldsymbol{\mu}_{k_n})$ containing the coefficients $\boldsymbol{\sigma}_j(\boldsymbol{\mu}_{k_n})$ is precomputed by solving a least-squares fitting problem.

2. Online stage: In this stage, the solution at a new parameter is approximated by solving the minimization problem (3.8).

3.2   Precomputation stage

The set of snapshots at sampled parameters $\boldsymbol{\mu}_s$, $s = 1, \cdots, N_s$ are stored in a snapshot matrix $\boldsymbol{M}$. The methodology for evaluation of the transport matrix $\boldsymbol{\Psi}(\boldsymbol{\mu}_s)$, $s = 1, \cdots, N_s$ for each snapshot is explained in this section.

The matrix $\boldsymbol{\Psi}(\boldsymbol{\mu}_s)$ containing the coefficients $\boldsymbol{\sigma}_j(\boldsymbol{\mu}_s)$ is constructed in such a way that a subset of solution snapshots $\boldsymbol{w}(\boldsymbol{\mu}_{v_n})$ for $n = 1, \cdots, N_v$, where $\boldsymbol{\mu}_{v_n} \in \boldsymbol{\mu}_s$, can be represented as the transported snapshot of $\boldsymbol{w}(\boldsymbol{\mu}_s)$. Here $\boldsymbol{\mu}_{v_n}$ are defined as the training parameters for $\boldsymbol{\mu}_s$ and the corresponding snapshots are called training snapshots. The procedure for selecting N_v training snapshots from N_s is described in Sec. 3.2.1. The transported snapshot denoted by $\boldsymbol{w}'(\boldsymbol{\mu}_s, \boldsymbol{\mu}_{v_n})$ is obtained by transformation of Cartesian coordinates as

explained in Sec. 3.1:

$$\boldsymbol{x}_i'(\boldsymbol{\mu}_s, \boldsymbol{\mu}_{v_n}) = \boldsymbol{x}_i + \boldsymbol{\sigma}(\boldsymbol{\Delta\mu}), \quad \text{for } i = 1, 2, 3, \text{ and } n = 1, \dots, N_v \tag{3.9}$$

The transport $\boldsymbol{\sigma}(\boldsymbol{\Delta\mu})$ is defined as a function of $\boldsymbol{\Psi}(\boldsymbol{\mu}_s)$ and $\boldsymbol{d}(\boldsymbol{\Delta\mu}_{sv_n})$ as described in Eqs. (3.5) and (3.6) (but with $\boldsymbol{\mu}_{k_n}$ replaced by $\boldsymbol{\mu}_s$; and $\boldsymbol{\Delta\mu} = (\boldsymbol{\mu}_{v_n} - \boldsymbol{\mu}_s) \oslash \boldsymbol{\Delta\mu}_d$ for $n = 1, \dots, N_v$).

Finally, the coefficients of Fourier expansion of $\boldsymbol{\sigma}_j(\boldsymbol{\mu}_s)$ are evaluated by minimizing the least-squares training error between the transported snapshot $\boldsymbol{w}'(\boldsymbol{\mu}_s, \boldsymbol{\mu}_{v_n})$ and training snapshot $\boldsymbol{w}(\boldsymbol{\mu}_{v_n})$:

$$\min_{\boldsymbol{c}^s} \sum_{n=1}^{N_v} \|\boldsymbol{w}'(\boldsymbol{\mu}_s, \boldsymbol{\mu}_{v_n}) - \boldsymbol{w}(\boldsymbol{\mu}_{v_n})\|_2^2 \tag{3.10}$$

where $\boldsymbol{c}^s := c_{p,q,r}^{s(l)}$ are the Fourier coefficients as described in Eq. (3.7). The optimization problem (3.10) is solved N_s times for the coefficients $\boldsymbol{c}^s$ to eventually construct the transport matrix $\boldsymbol{\Psi}(\boldsymbol{\mu}_s)$ for $s = 1, \cdots, N_s$ snapshots.

3.2.1 Choice of training snapshots, $\boldsymbol{w}(\boldsymbol{\mu}_{v_n})$

For a large class of parametric problems, we assume that the error between the transported snapshot $\boldsymbol{w}'(\boldsymbol{\mu}_s, \boldsymbol{\mu}_{v_n})$ and training snapshot $\boldsymbol{w}(\boldsymbol{\mu}_{v_n})$ for a fixed $\boldsymbol{\Psi}(\boldsymbol{\mu}_s)$ tends to increase as the parameter variation $\boldsymbol{\Delta\mu}$ increases. Hence N_v training snapshots are chosen which correspond to nearest sampled snapshots to $\boldsymbol{w}(\boldsymbol{\mu}_s)$ in parameter space. Nearest neighboring snapshots are defined as the snapshots $\boldsymbol{w}(\boldsymbol{\mu}_{v_n})$ for which $\Delta\mu = \|\boldsymbol{\Delta\mu}\|_2$ is minimum.

3.3 Online stage

In this stage, local reduced-basis $\boldsymbol{U}(\boldsymbol{\mu}^*)$ at an unsampled parameter $\boldsymbol{\mu}^* \neq \boldsymbol{\mu}_s$ is constructed and generalized coordinates $\boldsymbol{a}(\boldsymbol{\mu}^*)$ are calculated.

For a parameter $\boldsymbol{\mu}^*$ in the predictive regime, local reduced-basis $\boldsymbol{U}(\boldsymbol{\mu}^*)$ is constructed by collecting the transported snapshots of $\boldsymbol{w}(\boldsymbol{\mu}_{k_n})$ for $n = 1, \cdots, N_k$, where $\boldsymbol{\mu}_{k_n} \in \boldsymbol{\mu}_s$ is a subset of snapshot solutions, as shown in Eq. (3.11). The procedure for selecting $\boldsymbol{w}(\boldsymbol{\mu}_{k_n})$ is described in Sec. 3.3.1.

$$\boldsymbol{U}(\boldsymbol{\mu}^*) = [\boldsymbol{w}'(\boldsymbol{\mu}_{k_1}, \boldsymbol{\mu}^*); \boldsymbol{w}'(\boldsymbol{\mu}_{k_2}, \boldsymbol{\mu}^*); \cdots; \boldsymbol{w}'(\boldsymbol{\mu}_{k_{N_k}}, \boldsymbol{\mu}^*)] \tag{3.11}$$

The transported snapshots $\boldsymbol{w}'(\boldsymbol{\mu}_{k_n}, \boldsymbol{\mu}^*)$ are calculated by transformation of spatial coordinates based on the

transports in Eq. (3.5).

Finally, the generalized coordinates are obtained by solving the minimization problem (3.8). Initial guesses for the generalized coordinates $\boldsymbol{a}(\boldsymbol{\mu^*})^{(0)}$ are provided by assuming that the contribution from each transported snapshot is inversely proportional to their respective parameter variation $\Delta\mu = ||(\boldsymbol{\mu^*} - \boldsymbol{\mu}_{k_n}) \oslash \Delta\boldsymbol{\mu}_d||_2$ and sum of all such individual contributions equals one. Hence $\boldsymbol{a}(\boldsymbol{\mu^*})^{(0)}$ is given by (3.12):

$$a(\boldsymbol{\mu^*})_n^{(0)} = \frac{\frac{1}{\Delta\mu}}{\sum_{n=1}^{N_k} \frac{1}{\Delta\mu}} \tag{3.12}$$

3.3.1 Choice of basis

In traditional projection-based MOR applied to smooth elliptic problems, ROM performance is expected to improve by increasing the number of basis N_k. Unfortunately, this is usually not the case when the solutions of interest are characterized by strong shocks and discontinuities. For example, Abgrall et al. [41] demonstrate that optimal reconstructions of such solutions are typically sparse in the generalized coordinates and local in the parameter space. This property was also demonstrated in the toy problem considered in Sec. 2.4. Therefore, in this work, we use only a small number of local basis (transported snapshots) corresponding to nearest sampled snapshots selected from the set of N_s snapshots. Nearest neighboring snapshots are again defined as the snapshots $\boldsymbol{w}(\boldsymbol{\mu}_{k_n})$ for which the corresponding parameter variation $\Delta\mu$ is minimum.

3.4 Choice of norms, ℓ_p

In traditional projection-based MOR, the generalized coordinates are usually selected to minimize the ℓ_2-norm of the residual. Although this approach has been demonstrated to work adequately for many applications, in the case when the FOM is comprised of a system of hyperbolic conservation laws, minimizing the ℓ_1-norm has been shown to be preferable [41]. For our proposed approach, ℓ_1 norm for the residual minimization (3.8) is found to perform better than other choices of norms. Unfortunately, the optimal choice of norm remains an open problem.

The classical approach to solving ℓ_1-norm minimization problems involves recasting the problem as a linear program or, alternatively, solving iteratively using, for example, Iteratively Reweighted Least Squares (IRLS) [50, 51]. Methodology for minimizing ℓ_1-norm is also explained in [41].

3.5 Summary of TSMOR

The offline and online stages of the proposed TSMOR approach are summarized in Algorithms 1 and 2, respectively.

Algorithm 1 TSMOR-offline stage

Input: Steady state snapshots, $\boldsymbol{w}(\boldsymbol{\mu_s})$ for $s = 1, \ldots, N_s$

Output: $\boldsymbol{\Psi}(\boldsymbol{\mu}_s)$ for $s = 1, \ldots, N_s$

 1: **for** $s \leftarrow 1$ to N_s **do**

 2:    Determine N_v training snapshots $\boldsymbol{w}(\boldsymbol{\mu}_{v_n})$ for $n = 1, \ldots, N_v$ as mentioned in Sec. 3.2.1

 3:    Determine $\boldsymbol{\Delta\mu} = (\boldsymbol{\mu}_{v_n} - \boldsymbol{\mu}_s) \oslash \Delta\boldsymbol{\mu}_d$ for $n = 1, \ldots, N_v$

 4:    Define $\boldsymbol{d}(\boldsymbol{\Delta\mu})$ using Eq. (3.6)

 5:    Express $\boldsymbol{\Psi}(\boldsymbol{\mu}_s)$ as a Fourier series using Eq. (3.7)

 6:    Define transports $\boldsymbol{\sigma}(\boldsymbol{\Delta\mu})$ using Eq. (3.5)

 7:    Compute transported snapshots $\boldsymbol{w}'(\boldsymbol{\mu}_s, \boldsymbol{\mu}_{v_n})$ from Eq. (3.9) in Lagrangian frame of reference

 8:    Solve training error minimization problem (3.10) for Fourier coefficients $\boldsymbol{c}^s$

 9:    Evaluate $\boldsymbol{\Psi}(\boldsymbol{\mu}_s)$ using Eq. (3.7)

10: **end for**

Algorithm 2 TSMOR-online stage

Input: $\boldsymbol{w}(\boldsymbol{\mu_s})$ and $\boldsymbol{\Psi}(\boldsymbol{\mu}_s)$ for $s = 1, \ldots, N_s$; Unsampled parameter, $\boldsymbol{\mu}^*$

Output: Solution prediction, $\boldsymbol{w}_r(\boldsymbol{\mu}^*)$

 1: Determine N_k local snapshots $\boldsymbol{w}(\boldsymbol{\mu}_{k_n})$ for $k = 1, \ldots, N_k$ as mentioned in Sec. 3.3.1

 2: Determine $\boldsymbol{\Delta\mu} = (\boldsymbol{\mu}^* - \boldsymbol{\mu}_{k_n}) \oslash \Delta\boldsymbol{\mu}_d$ for $k = 1, \ldots, N_k$

 3: Define $\boldsymbol{d}(\boldsymbol{\Delta\mu})$ using Eqs. (3.6)

 4: Compute transports $\boldsymbol{\sigma}(\boldsymbol{\Delta\mu})$ using Eq. (3.5)

 5: Compute transported snapshots $\boldsymbol{w}'(\boldsymbol{\mu}_{k_n}, \boldsymbol{\mu}^*)$ from Eq. (3.2) in Lagrangian frame of reference

 6: Construct local basis $\boldsymbol{U}(\boldsymbol{\mu}^*)$ using Eq. (3.11)

 7: Solve residual minimization problem (3.8) for $\boldsymbol{a}(\boldsymbol{\mu}^*)$

 8: Compute $\boldsymbol{w}_r(\boldsymbol{\mu}^*)$ from Eq. (3.1)

Chapter 4

Hyper-reduction

In the online stage of TSMOR, evaluation of residuals $\boldsymbol{R}(\boldsymbol{U}(\boldsymbol{\mu^*})\boldsymbol{a}(\boldsymbol{\mu^*}))$ in Eq. (3.8) scales with the size of the FOM, N_w. Hyper-reduction can significantly reduce this computational complexity. A review of the state of art hyper-reduction techniques, such as DEIM [52], GNAT [53] and ECSW [54] is provided in this chapter. Furthermore, the methodology to equip the proposed TSMOR approach with hyper-reduction strategies is outlined.

4.1   Review of hyper-reduction techniques

In hyper-reduction, the residual is evaluated only at a small subset of n_w interpolation entries $\varepsilon \subset \{1, \cdots, N_w\}$. The interpolation matrix $\boldsymbol{Z} \in \mathbb{R}^{N_w \times n_w}$ is thus defined as

$$\boldsymbol{Z} = [\boldsymbol{e}_{\varepsilon_1}, \boldsymbol{e}_{\varepsilon_2}, \cdots, \boldsymbol{e}_{\varepsilon_{n_w}}] \tag{4.1}$$

where $\boldsymbol{e}_\varepsilon$ is the εth canonical unit vector. $\boldsymbol{R}(\boldsymbol{U}\boldsymbol{a}^{(i)})$ is then approximated in a low dimensional subspace $\boldsymbol{U}_R \in \mathbb{R}^{N_w \times N_R}$

$$\boldsymbol{R}(\boldsymbol{U}\boldsymbol{a}^{(i)}) \approx \boldsymbol{U}_R(\boldsymbol{Z}^T\boldsymbol{U}_R)^+ \boldsymbol{Z}^T \boldsymbol{R}(\boldsymbol{U}\boldsymbol{a}^{(i)}) \tag{4.2}$$

Finally, equation (4.2) is projected in a low-dimensional subspace using state basis $\boldsymbol{U}$. Thus the resulting minimization problem is independent of the size of FOM, N_w.

Another class of hyper-reduction techniques, for instance ECSW, involves minimization of the weighted residuals computed only at ε points. Thus, all the computations are performed on these *collocation points* and interpolation of the residuals using basis functions is avoided.

4.2 Hyper-reduction applied to TSMOR

In this work, we adopt a collocation-based hyper-reduction approach similar to ECSW. More specifically, the residual minimization problem (3.8) in this hyper-reduction framework is written as

$$\min_{\boldsymbol{a}}\|\boldsymbol{Z}^T\boldsymbol{R}(\boldsymbol{U}(\boldsymbol{\mu}^*)\boldsymbol{a}(\boldsymbol{\mu}^*);\boldsymbol{\mu}^*)\|_p \tag{4.3}$$

Generally, in most CFD problems, the Jacobian matrix is sparse. Hence the computation of the residuals is dependent only on a few subset of $\hat{n}_w$ entries $\hat{\varepsilon}\subset\{1,\cdots,N_w\}$. The corresponding interpolation matrix is denoted as $\boldsymbol{P}$. Thus $\boldsymbol{U}\boldsymbol{a}^{(i)}$ can be replaced by $\boldsymbol{P}\boldsymbol{P}^T\boldsymbol{U}\boldsymbol{a}^{(i)}$. But since our proposed approach requires online computation of parameter dependent basis $\boldsymbol{U}(\boldsymbol{\mu}^*)$ for every new prediction, this computation still scales with the size N_w. To tackle this issue, the local basis, which is essentially a matrix of transported snapshots, are also calculated only at $\hat{\varepsilon}$ indices. The transported snapshot at collocated points is computed in a Lagrangian frame of reference where the new particle locations at collocated points are given by:

$$\hat{\boldsymbol{x}}_i(\boldsymbol{\mu}_{k_n},\boldsymbol{\mu}^*)=\hat{\boldsymbol{x}}_i+\hat{\boldsymbol{\sigma}}(\boldsymbol{\Delta\mu}),\quad \text{for } i=1,2,3, \text{ and } n=1,\ldots,N_k \tag{4.4}$$

where $\hat{\boldsymbol{\sigma}}(\boldsymbol{\Delta\mu})=\boldsymbol{P}^T\boldsymbol{\sigma}(\boldsymbol{\Delta\mu})\in\mathbb{R}^{\hat{n}_w}$ are the collocated transports and $\hat{\boldsymbol{x}}_i=\boldsymbol{P}^T\boldsymbol{x}_i\in\mathbb{R}^{\hat{n}_w}$ and $\hat{\boldsymbol{x}}_i(\boldsymbol{\mu}_{k_n},\boldsymbol{\mu}^*)\in\mathbb{R}^{\hat{n}_w}$ are the Cartesian coordinates of the original and transported parcels at the collocation points, respectively.

To summarize, equation (4.3) involves computation of $\boldsymbol{Z}^T\boldsymbol{R}(\boldsymbol{P}\boldsymbol{P}^T\boldsymbol{U}(\boldsymbol{\mu}^*)\boldsymbol{a}(\boldsymbol{\mu}^*))$ which necessitates the computation of $\boldsymbol{R}(\boldsymbol{U}(\boldsymbol{\mu}^*)\boldsymbol{a}(\boldsymbol{\mu}^*))$ and $\boldsymbol{U}(\boldsymbol{\mu}^*)$ only at ε and $\hat{\varepsilon}$ indices respectively, resulting in a reduction of computational complexity from N_w to $\hat{n}_w$.

4.3 Identification of collocation points

Various hyper-reduction techniques in literature employ different strategies for identifying the collocation points or interpolation entries ε. Generally, these approaches are specific to their respective hyper-reduction procedure. For instance, these algorithms are based on minimization of the error in the interpolated snapshots [52], greedy approach to minimize error associated with gappy-POD projection of residual [55] and solving a sparse non-negative least squares (NNLS) problem [54]. In this work, we employ the standard DEIM algorithm 3 to identify the collocation points.

The standard DEIM algorithm uses basis functions $\boldsymbol{U}_R$ of the nonlinear residual to identify the interpolation entries ε. In our implementation of the algorithm, $\boldsymbol{U}_R$ are the POD basis of the snapshots of residuals. The snapshots of residuals are collected at each iteration or time-step while solving the FOM Eq. 2.2 during the

precomputation stage. For boundary value problems, in addition to DEIM indices, it is important to include inlet/outlet grid points into ε since these boundary conditions contain vital information about dynamics of the problem. Details about inclusion of these boundary points are explained in Chapter 5 where this topic is covered for each flow problem. Finally, corresponding interpolation entries $\hat{\varepsilon}$ for computing the residuals can be related to ε depending on the type of finite-difference/volume/element scheme.

Algorithm 3 DEIM

Input: POD basis of snapshots of Residuals, $\boldsymbol{U}_R$

Output: Interpolation entries $\vec{\varepsilon} = [\varepsilon_1, \cdots, \varepsilon_{n_w}]$

1: $[\ , \varepsilon_1] = \texttt{max}\{|\boldsymbol{U}_{R_{(:,l)}}|\}$

2: $\boldsymbol{V} = [\boldsymbol{U}_{R_{(:,l)}}]$, $\boldsymbol{Z} = [\boldsymbol{e}_{\varepsilon_1}]$, $\vec{\varepsilon} = [\varepsilon_1]$

3: **for** $l \leftarrow 2$ to n_w **do**

4:    Solve $(\boldsymbol{Z}^T \boldsymbol{V}) c = \boldsymbol{P}^T \boldsymbol{U}_{R_{(:,l)}}$

5:    $\boldsymbol{r} = \boldsymbol{U}_{R_{(:,l)}} - \boldsymbol{V} \boldsymbol{c}$

6:    $[\ , \varepsilon_l] = \texttt{max}\{|\boldsymbol{r}|\}$

7:    $\boldsymbol{V} \leftarrow [\boldsymbol{V}, \boldsymbol{U}_{R_{(:,l)}}]$, $\boldsymbol{Z} \leftarrow [\boldsymbol{Z}, \boldsymbol{e}_{\varepsilon_l}]$, $\vec{\varepsilon} \leftarrow [\vec{\varepsilon}, \varepsilon_l]$

8: **end for**

Chapter 5

Numerical experiments

In this chapter, TSMOR is applied to the steady Euler equations modeling supersonic flow inside a quasi 1-D nozzle and 2-D flow over a forward facing step and a nonlinear advection-diffusion equation modeling a jet diffusion flame in a combustor. These problems are chosen because the steady flow solutions contain shocks or flame fronts whose spatial locations and orientations are parameter dependent. Similar numerical experiments have been studied by Lucia et al. [45], Mojgani and Balajewicz [44], Zahr et al. [24]; Welper [56]; and Galbally et al. [57] respectively.

In this chapter, the results generated by the proposed TSMOR approach are compared with traditional projection-based MOR techniques such as least-squares Petrov-Galerkin (LSPG) methods as described in Sec. 2.2. Furthermore, comparison is also made with recent parametric MOR techniques such as L_1-dictionary approach [41] where the solution is given by a linear combination of local snapshots or *dictionary* elements and L_1-norm of the residual is minimized. All results considered in this chapter are predictive, that is, the predicted solutions all lie in parameter regions not sampled during the offline training phase. The performance of these MOR techniques are analyzed by computing the relative error between the predicted and full order model solutions where the error is defined as:

$$Error(\%) = \frac{||\boldsymbol{w}(\boldsymbol{\mu}^*) - \boldsymbol{w}_r(\boldsymbol{\mu}^*)||_2}{||\boldsymbol{w}(\boldsymbol{\mu}^*)||_2} \times 100 \tag{5.1}$$

where $\boldsymbol{w}(\boldsymbol{\mu}^*)$ and $\boldsymbol{w}_r(\boldsymbol{\mu}^*)$ are the FOM and predicted solutions using the above-mentioned MOR methods, respectively. All the computations were done in Matlab.

5.1 Quasi 1-D flow in a converging-diverging nozzle

5.1.1 Problem description

The 1-D Euler equations in a quasi 1-D converging-diverging nozzle are considered:

$$\frac{1}{A}\frac{\partial A\boldsymbol{F}}{\partial x} = \boldsymbol{Q} \qquad x \in [0, L] \tag{5.2}$$

where $A = A(x)$ is the area profile and

$$\boldsymbol{w}(\mu) = \begin{bmatrix} \rho \\ \rho u \\ \rho E \end{bmatrix}, \quad \boldsymbol{F} = \begin{bmatrix} \rho u \\ \rho u^2 + p \\ (\rho E + p)u \end{bmatrix}, \quad \boldsymbol{Q} = \begin{bmatrix} 0 \\ \frac{p}{A}\frac{\partial A}{\partial x} \\ 0 \end{bmatrix}$$

with homogeneous Dirichlet boundary conditions $\rho(0; \mu) = 1$, $p(0; \mu) = 1$ and $p(L; \mu) = 0.7$.
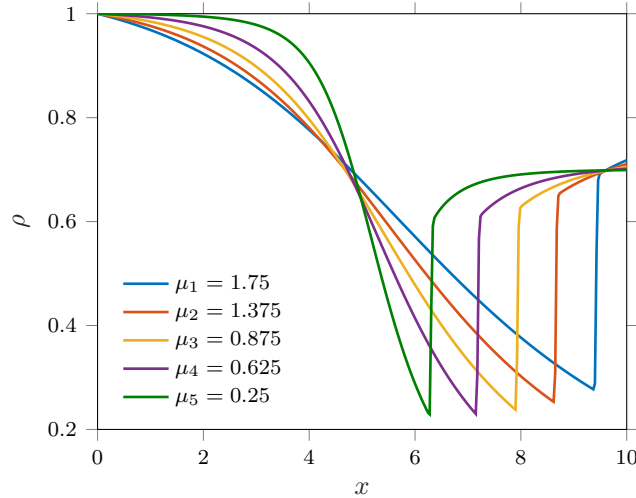
Figure 5.1: Steady density solution ρ for various throat area parameters $\boldsymbol{\mu}$

The boundary conditions are chosen such that a shock is formed in the diverging section of the nozzle. Length of the nozzle L is 10 units. Area profile of the converging-diverging nozzle is parabolic with equal inlet and outlet area, $A(0) = A(L) = 3$, and the throat is located at $L/2$. For this problem, the throat area $\mu = A(L/2)$ is the parameter of interest. Steady state solutions are obtained by discretizing the corresponding governing equations in space using a central second-order finite difference scheme on a uniform grid with grid spacing $\Delta x = 0.01$. A first-order accurate artificial viscosity scheme using $\nu = \Delta x/2$ is used to stabilize the solution. The resulting nonlinear system of algebraic equations is solved in Matlab using the built-in `fsolve` algorithm. Fig. 5.1 shows the steady density solutions for different values of throat area μ.

5.1.2 Implementation of TSMOR

A snapshot matrix M containing 4 snapshots at parameters $\mu_s = [0.5, 0.875, 1.25, 1.625]$ is generated. Transport matrices for each snapshot $\mathbf{\Psi}(\mu_s)$ are computed offline by solving the training error minimization (3.10). They are expressed as a Fourier sine series with three modes ($m = 3$):

$$\mathbf{\Psi}(\mu_s)_{(:,j)} = c_0^{s(j)} + \sum_{p=1}^{p=m-1} c_p^{s(j)} \sin\left(\frac{p\pi \boldsymbol{x}}{L}\right) \tag{5.3}$$

where $\boldsymbol{c}^{s(j)}$ are the coefficients of Fourier expansion. For this simple toy problem, $d(\Delta\mu)$ is given by:

$$d(\Delta\mu) = \Delta\mu \tag{5.4}$$

The interpolation from the transported grid to the original Eulerian grid for calculating the transported snapshots was performed using `interp1` algorithm. The training error minimization (3.10) is solved using `fmincon` algorithm where the Eq. (3.10) is subjected to the constraint of no-grid entanglement: $V_j > \delta_v$ for $j = 1, \ldots, N_V$ where V_j are the N_V element volumes and $\delta_v > 0$ is the minimal positive volume. For a structured Cartesian grid, this constraint simplifies to $x_i'(\mu_{k_n}, \mu^*)_{j+1} - x_i'(\mu_{k_n}, \mu^*)_j > \delta_v$ for $i = 1, 2, 3$ and $j = 1, \ldots, N_w - 1$.

Fig. 5.2 illustrates the predictive capabilities of several MOR approaches for the parameter $\mu^* = 1.0$ and $\mu^* = 1.5$. The FOM is given by the gray lines while the new proposed TSMOR approach using 2 local basis corresponding to two nearby snapshots is given by the red lines. The blue lines correspond to the solution obtained by LSPG method using 4 POD modes of the snapshot matrix M. The green lines correspond to L_1-dictionary approach using 2 local snapshots or dictionary elements. The proposed TSMOR approach reproduces the solution remarkably well. In contrast, LSPG does not predict the correct shock location while L_1-dictionary solutions are dominated by staircase shock type errors.

Next, the TSMOR approach is equipped with the hyper-reduction strategy mentioned in Sec. 4.2. First, 30 collocation points are obtained by employing the DEIM algorithm. Second, these points are augmented with inlet and outlet points, $i = 1$, and $i = N_w$, respectively. Finally, an additional $\hat{n}_w \approx n_w \times 2 = 64$ points $\hat{\varepsilon}$ are included to enable the evaluation of the residuals via the central finite difference scheme. Figs. 5.3 and 5.4 illustrate the predictive capabilities of hyper-reduced TSMOR (TSMOR+HR) for the same parameters $\mu^* = 1.0$ and $\mu^* = 1.5$, respectively. The hyper-reduced TSMOR solutions are compared with non-hyper-reduced LSPG and L_1-dictionary approaches. As before, excellent agreement with the FOM solution is demonstrated by hyper-reduced TSMOR.
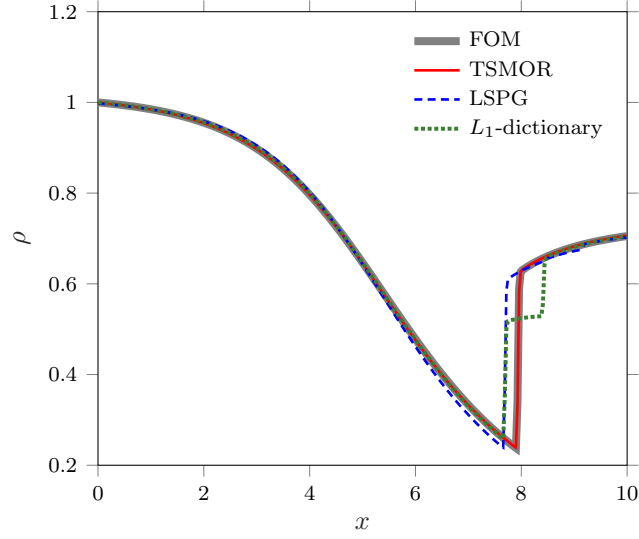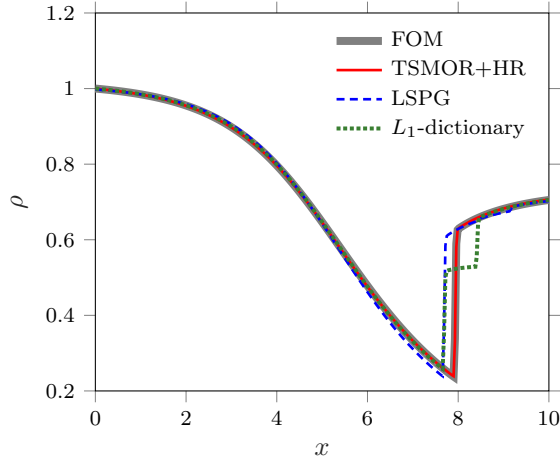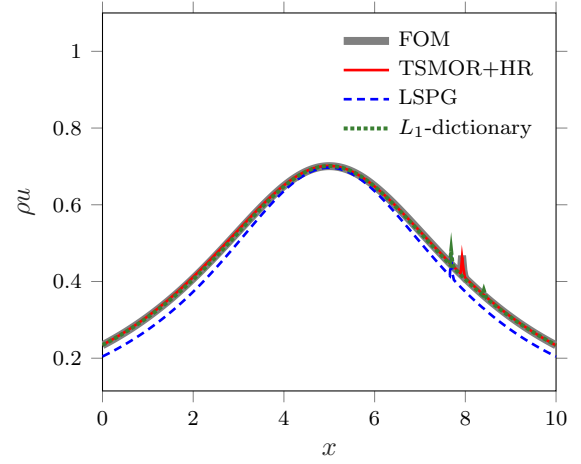
(a) Predicted solutions at $\mu^* = 1.0$
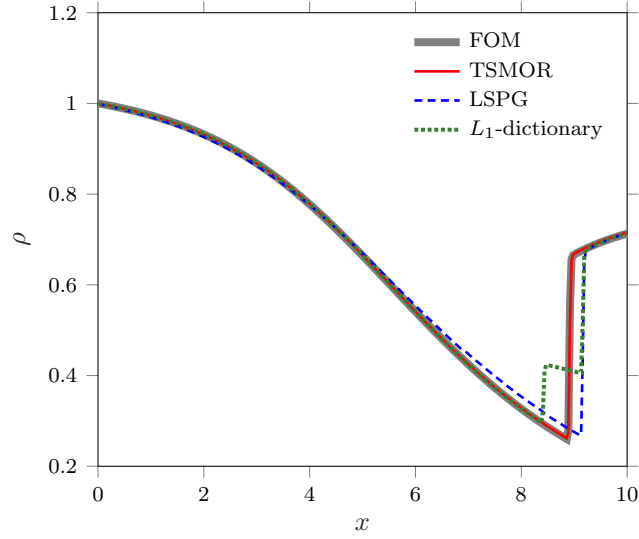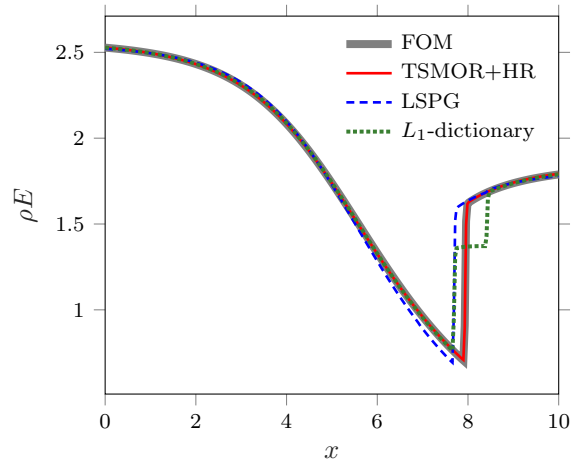

(b) Predicted solutions at $\mu^* = 1.5$

Figure 5.2: Comparison of predicted solutions using TSMOR, LSPG and L_1-dictionary approach with FOM
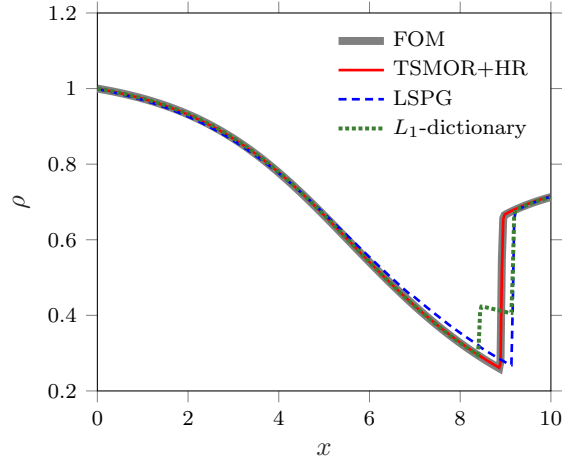
(a) Density solution

(b) x-momentum solution
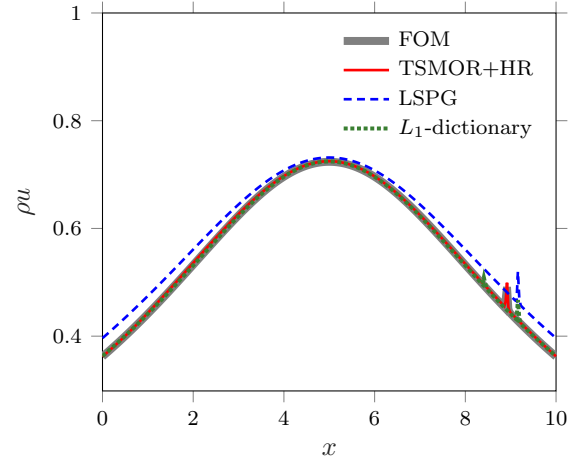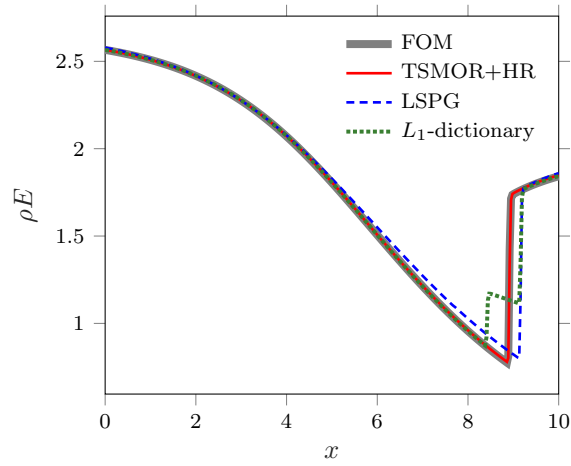

(c) Energy solution

Figure 5.3: Comparison of predicted solution at $\mu^* = 1.0$ using hyper-reduced TSMOR, LSPG and L_1-dictionary approach with FOM

(a) Density solution

(b) x-momentum solution

(c) Energy solution

Figure 5.4: Comparison of predicted solution at $\mu^* = 1.5$ using hyper-reduced TSMOR, LSPG and L_1-dictionary approach with FOM

In Fig. 5.5, relative errors between the FOM solutions and predicted solutions using hyper-reduced TSMOR, LSPG and L_1-dictionary approaches are illustrated across the entire parameter range of interest. For this case, predictions are made at two uniformly distributed parameters in every interval of μ_s. It can be observed that the solutions predicted using TSMOR have an average error of only 0.27% as compared to 7.22% in LSPG and 5.88% in L_1-dictionary approach. Thus, for all parameters considered, the TSMOR approach significantly outperforms LSPG and L_1-dictionary methods. Finally, wall-times and speed-ups are illustrated in Fig. 5.6a and Fig. 5.6b, respectively. TSMOR+HR delivers a speed-up of approximately four orders of magnitude across the entire parameter range while maintaining a high level of accuracy.
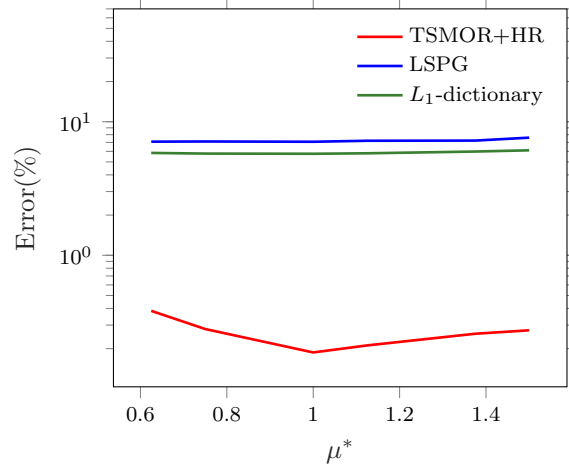
Figure 5.5: Performance comparison between hyper-reduced TSMOR, LSPG and L_1-dictionary approach for solution predictions at various parameters

(a) Wall-time

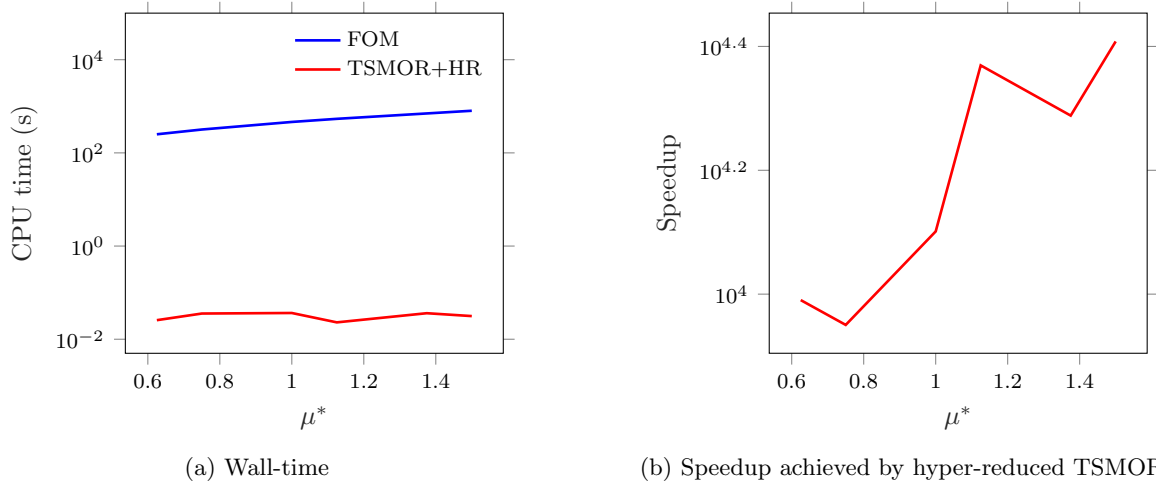(b) Speedup achieved by hyper-reduced TSMOR

Figure 5.6: Comparison of wall-times and speed-ups associated with FOM and online stage of hyper-reduced TSMOR for solution predictions at various parameters

5.2 Supersonic flow over a forward facing step

5.2.1 Problem description

This problem consists of a supersonic flow over a 2-D forward facing step in a wind tunnel setup with walls on top and bottom as described by [58] and also shown in Fig. 5.7. Length (L) and height (H) of the wind tunnel are 3 units and 1 unit respectively. The step has a height of 0.2 units and is located at the bottom wall starting at 0.6 units from the left-end of the tunnel. 2-D Euler equations governing the supersonic flow over a forward facing step are:

$$\frac{\partial \boldsymbol{F}}{\partial x} + \frac{\partial \boldsymbol{G}}{\partial y} = 0, \qquad x \in [0, L], \quad y \in [0, H], \quad \forall t > 0 \tag{5.5}$$

where

$$\boldsymbol{w}(\mu) = \begin{bmatrix} \rho \\ \rho u \\ \rho v \\ \rho E \end{bmatrix}; \boldsymbol{F} = \begin{bmatrix} \rho u \\ \rho u^2 + p \\ \rho uv \\ (\rho E + p)u \end{bmatrix}; \boldsymbol{G} = \begin{bmatrix} \rho v \\ \rho uv \\ \rho v^2 + p \\ (\rho E + p)v \end{bmatrix}$$

with homogeneous Dirichlet boundary conditions $\rho(0, y; \mu) = 1.4$, $p(0, y; \mu) = 1$, $u(0, y; \mu) = \mu$ and $v(0, y; \mu) = 0$; where μ is the inlet supersonic Mach number which is taken to the varying parameter of interest. No penetration solid wall boundary conditions are imposed on the top, bottom and step wall surfaces. The equations are discretized in space using a second-order, central finite difference scheme on a uniform Cartesian grid which is divided into 0.48 million grid points with $\Delta x = \Delta y = 0.025$. The solutions are stabilized using a first-order artificial viscosity scheme where the artificial viscosity is set to be $\nu = \Delta x / 0.8$. The resulting equations are solved by marching to steady state using a second-order Strong Stability Preserving (SSP) Runge–Kutta scheme [59]. Figs. 5.7a and 5.7b show the steady state density contour for inlet Mach number $\mu = 3.3$ and $\mu = 3.9$, respectively, while the corresponding 1-D plots at $y = 0.7$ are shown in Fig. 5.7c.
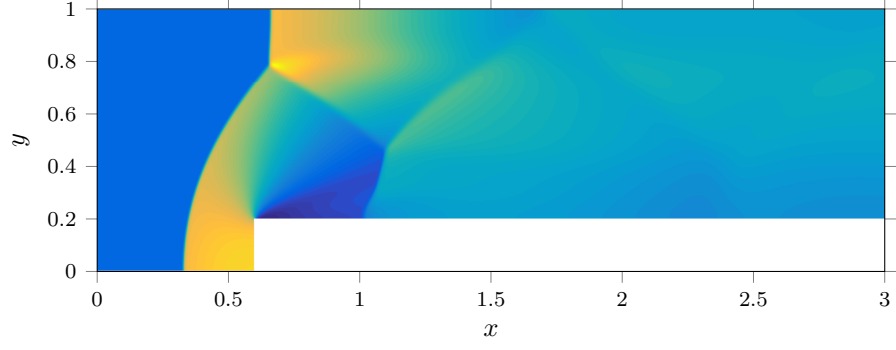
(a) Steady density contour for inlet Mach number $\mu = 3.3$
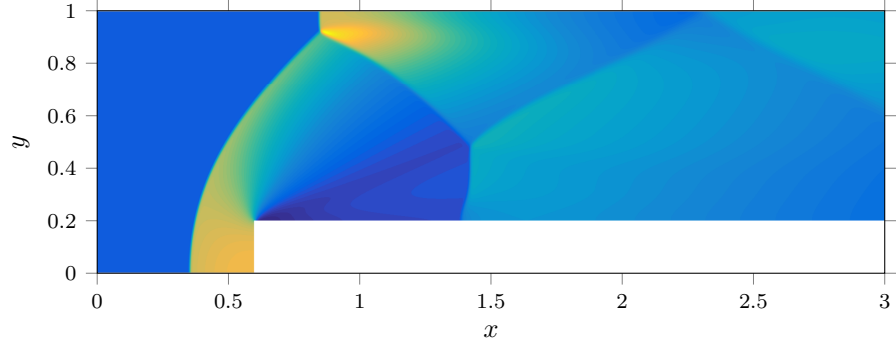
(b) Steady density contour for inlet Mach number $\mu = 3.9$
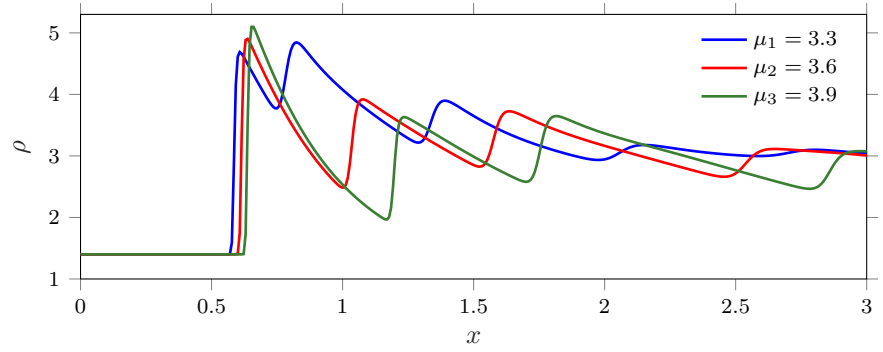
(c) 1-D steady density plot at $y = 0.7$ for inlet Mach number μ

Figure 5.7: Steady state density plots of supersonic flow over a forward facing step

5.2.2   Implementation of TSMOR

A snapshot matrix $\boldsymbol{M}$ containing 5 snapshots at parameters $\mu_s = [3.3, 3.45, 3.6, 3.75, 3.9]$ is generated. Transport matrices for each snapshot $\boldsymbol{\Psi}(\mu_s)$ are computed offline by solving the training error minimization (3.10). They are expressed as a Fourier sine series with 9 modes each ($m = 9$):

$$\boldsymbol{\Psi}_x(\mu_s)_{(:,j)} = c_{x_0}^{s(j)} + \sum_{p=1}^{p=m-1} c_{x_p}^{s(j)} \sin\left(\frac{p\pi\boldsymbol{x}}{L}\right) \tag{5.6}$$

$$\boldsymbol{\Psi}_y(\mu_s)_{(:,j)} = c_{y_0}^{s(j)} + \sum_{p=1}^{p=m-1} c_{y_p}^{s(j)} \sin\left(\frac{p\pi\boldsymbol{y}}{H}\right) \tag{5.7}$$

where $\boldsymbol{c}^{s(l)}$ are the coefficients of Fourier expansion. $\boldsymbol{d}(\Delta\mu)$ is given by:

$$\boldsymbol{d}(\boldsymbol{\Delta\mu}) = \begin{bmatrix} \Delta\mu \\ \Delta\mu^2 \end{bmatrix} \tag{5.8}$$

The interpolation from the transported grid to the original Eulerian grid for calculating the transported snapshots was performed using `interp2` algorithm in Matlab. The training error minimization (3.10) is solved using the `fmincon` algorithm subjected to the no-grid entanglement constraint as described in Sec. 5.1.2.

Fig. 5.8 illustrates the predictive capabilities of several MOR approaches for the parameter $\mu^* = 3.4$. The FOM solution is shown in Fig. 5.8a while the new proposed TSMOR solution using 2 local basis corresponding to two nearby snapshots is shown in Fig. 5.8b. Fig. 5.8c corresponds to the solution obtained by LSPG using 4 POD modes of the snapshot matrix $\boldsymbol{M}$. Fig. 5.8d corresponds to L_1-dictionary approach using 2 local basis or dictionary elements. The proposed TSMOR approach significantly out performs the LSPG and L_1-dictionary MOR approaches.
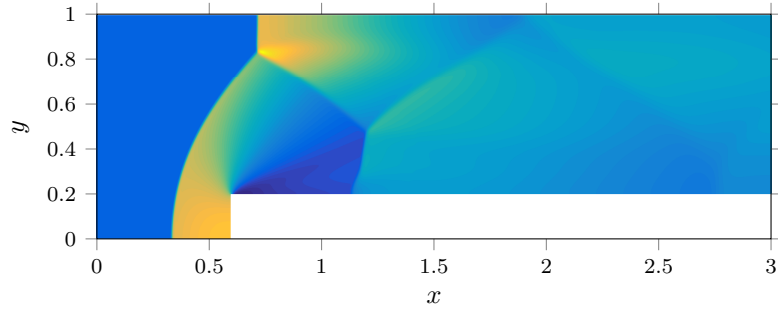
The predicted density, momentum and energy distributions at various y-locations for the FOM, TSMOR, LSPG and L_1-dictionary approaches are shown in Figs. 5.9- 5.12. As before, the TSMOR approach significantly outperforms LSPG and $L1$-dictionary methods.
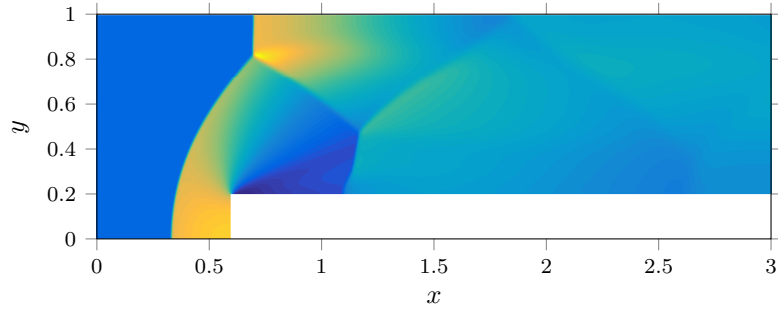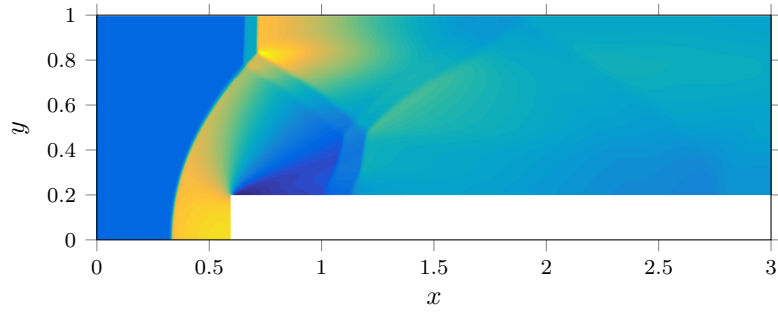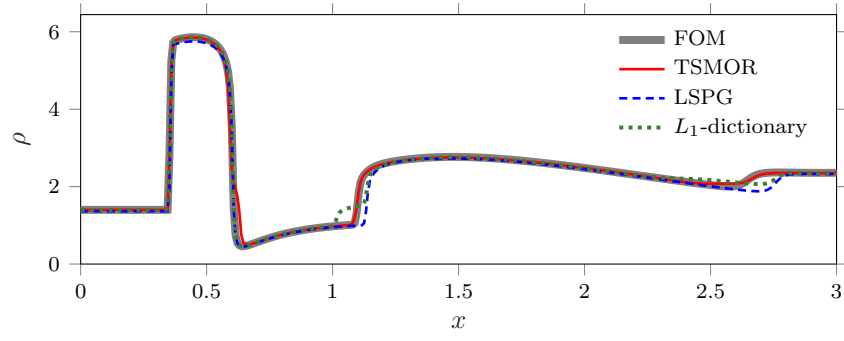
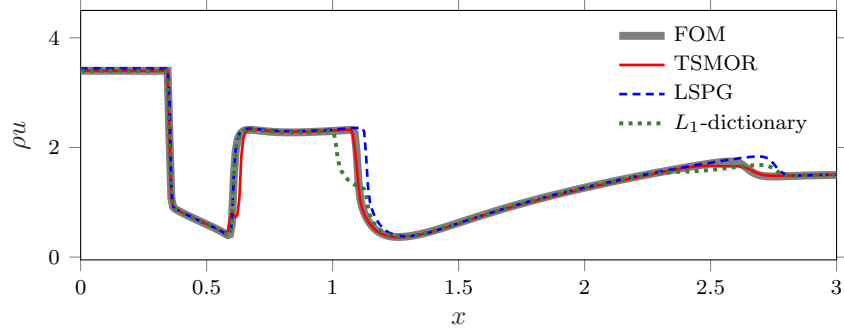(a) FOM solution
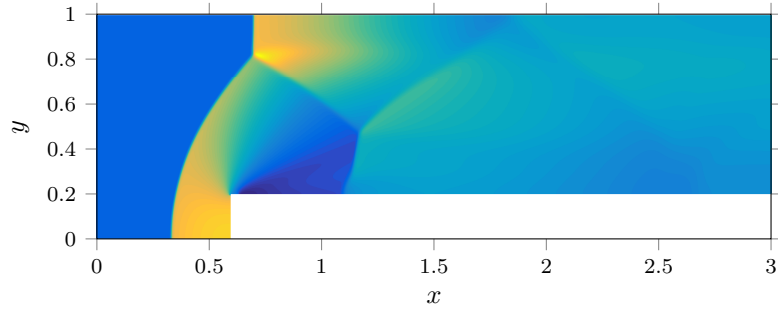
(b) TSMOR solution
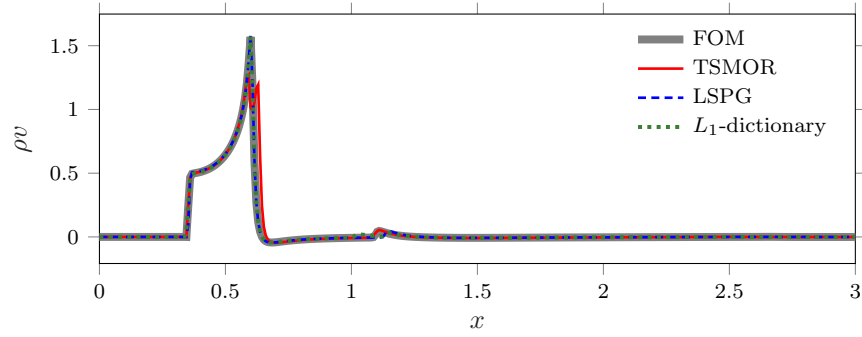

(c) LSPG solution

(d) L_1-dictionary solution

Figure 5.8: Comparison of steady state density solutions at $\mu^* = 3.4$ predicted by TSMOR, LSPG and L_1-dictionary approaches with FOM solution
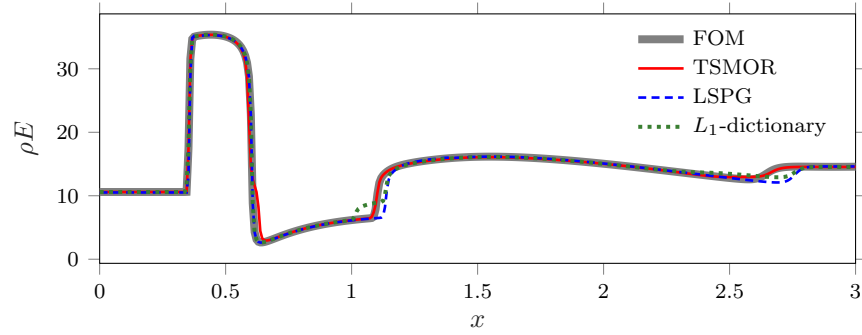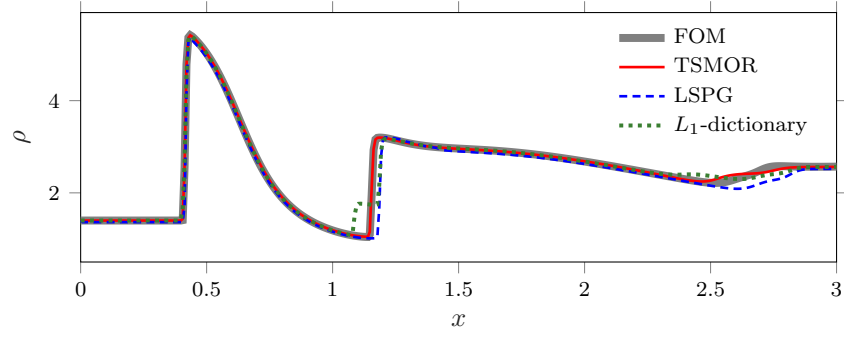
(a) Density solution

(b) x-momentum solution

(c) y-momentum solution

(d) Energy solution

Figure 5.9: 1D plots of solutions predicted by FOM, TSMOR, LSPG and L_1-dictionary approaches at $y = 0.205$

(a) Density solution

(b) x-momentum solution

(c) y-momentum solution

(d) Energy solution

Figure 5.10: 1D plots of solutions predicted by FOM, TSMOR, LSPG and L_1-dictionary approaches at $y = 0.4$

(a) Density solution

(b) x-momentum solution

(c) y-momentum solution
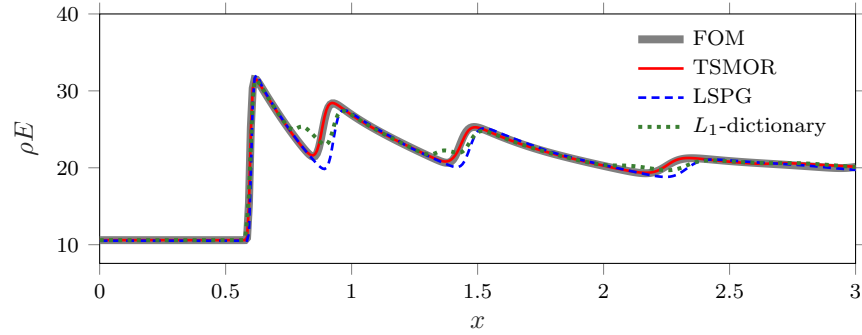
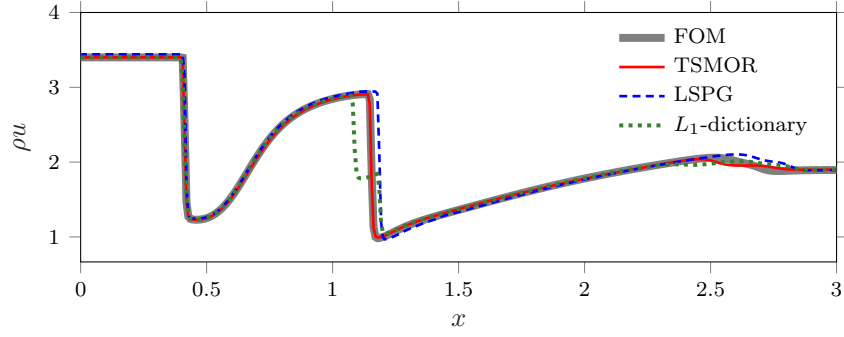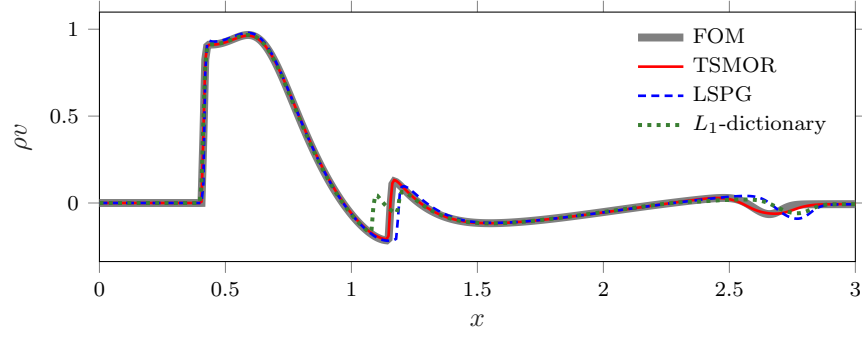
(d) Energy solution

Figure 5.11: 1D plots of solutions predicted by FOM, TSMOR, LSPG and L_1-dictionary approaches at $y = 0.7$
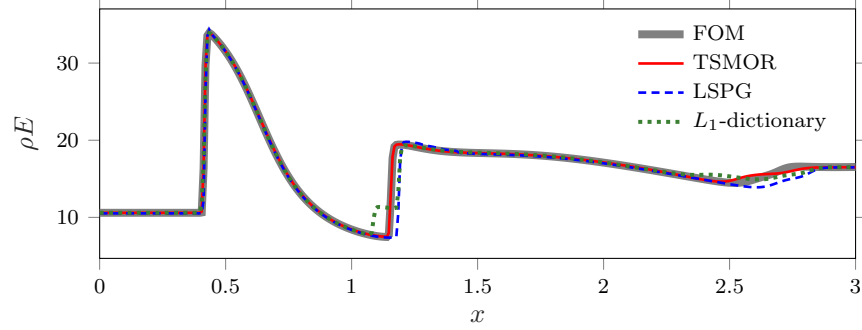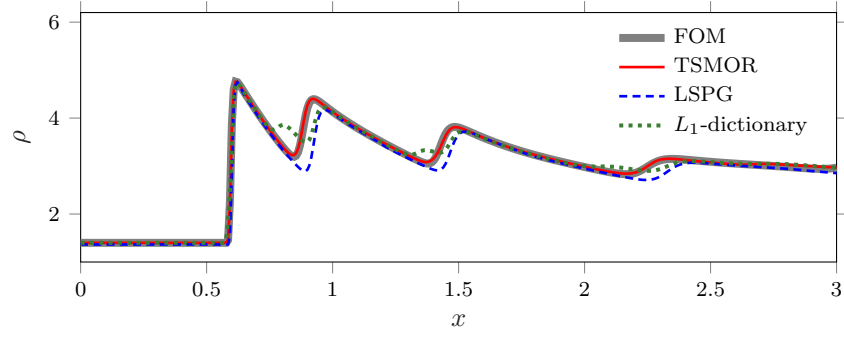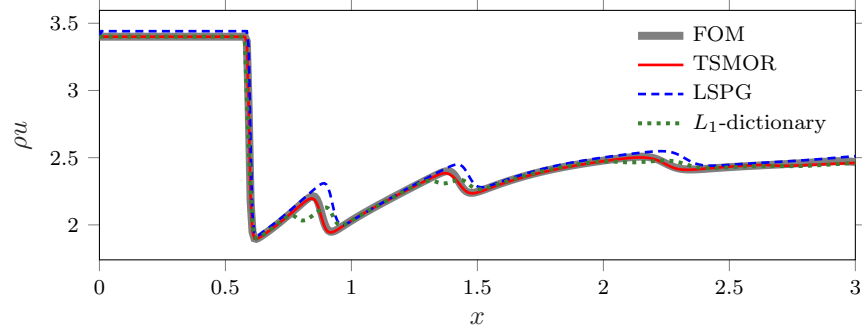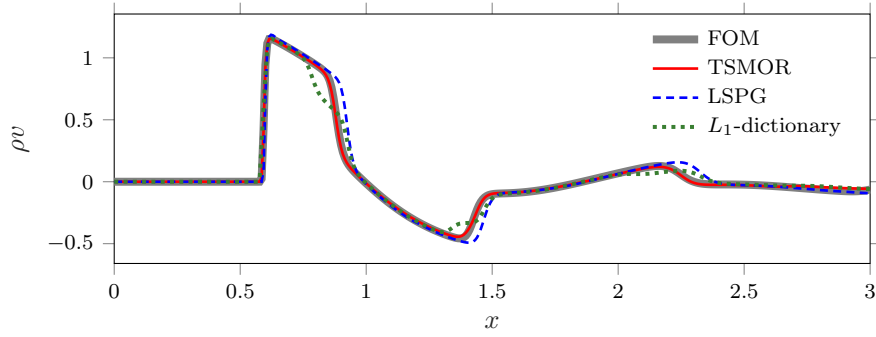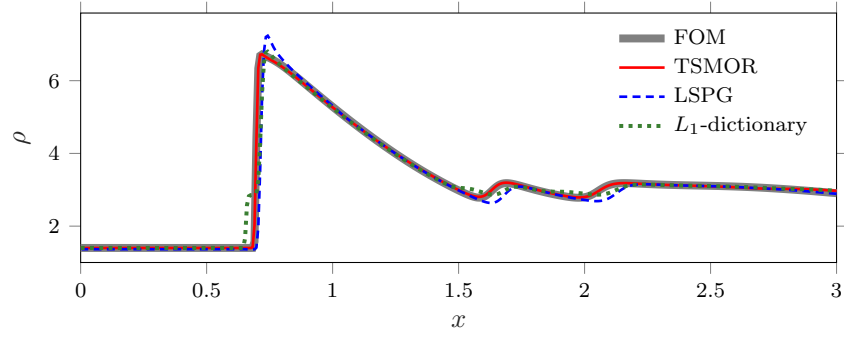
(a) Density solution
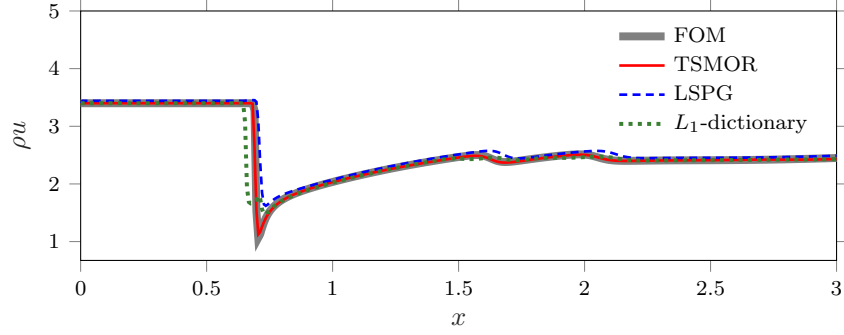
(b) x-momentum solution
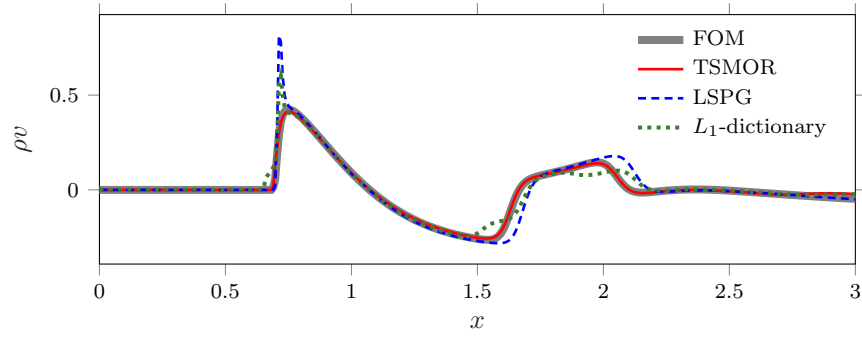
(c) y-momentum solution
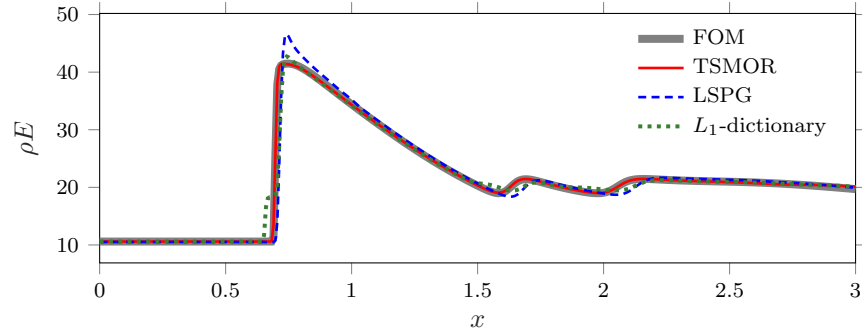
(d) Energy solution

Figure 5.12: 1D plots of solutions predicted by FOM, TSMOR, LSPG and L_1-dictionary approaches at $y = 0.83$

Finally, the relative solution errors between the FOM solutions and predicted solutions using TSMOR, LSPG and L_1-dictionary approaches across the entire parameter range of interest is given in Fig. 5.13. For this case, predictions are made at two uniformly distributed parameters in every interval of μ_s. It can be observed that the solutions predicted using TSMOR have an average error of only 0.6% as compared to 5.9% in LSPG and 5.0% in L_1-dictionary approach. Thus, for all parameters considered, the TSMOR approach outperforms LSPG and L_1-dictionary.
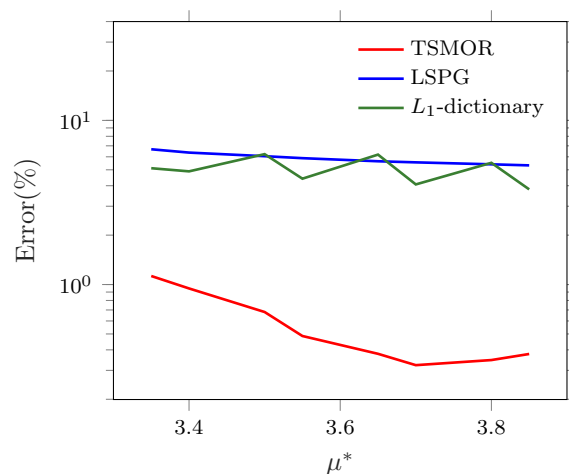
Figure 5.13: Performance comparison between TSMOR, LSPG and L_1-dictionary approaches for solution predictions at various parameters

5.3   Jet diffusion flame in a combustor

5.3.1   Problem description

This problem consists of jets of fuel and oxidizer injected into a combustion chamber as shown in Fig 5.14. Length (L) and height (H) of the chamber are 18 mm and 9 mm respectively. The width of fuel and oxidizer inlets are given denoted by H_f and H_o respectively. Inside the chamber, the fuel and oxidizer diffuse to form a diffusion flame where the combustion reaction is governed by an advection-diffusion type governing equation:

$$\nabla \cdot (\boldsymbol{W}\boldsymbol{w}(\boldsymbol{\mu})) - \nabla \cdot (\nu\nabla\boldsymbol{w}(\boldsymbol{\mu})) + \boldsymbol{f}(\boldsymbol{w}(\boldsymbol{\mu})) = 0 \qquad x \in [0, L], \quad y \in [0, H] \qquad (5.9)$$

where the state variable $\boldsymbol{w}(\boldsymbol{\mu})$ represents the concentration of fuel in the chamber, $\boldsymbol{W} = W_x\hat{i} + W_y\hat{j}$ is the velocity field and ν is the diffusion coefficient. The non-linear reaction term $\boldsymbol{f}(\boldsymbol{w}(\boldsymbol{\mu}))$ is of Arrhenius type given by:

$$\boldsymbol{f}(\boldsymbol{w}(\boldsymbol{\mu})) = A\boldsymbol{w}(\boldsymbol{\mu})(c - \boldsymbol{w}(\boldsymbol{\mu}))e^{-E/(d-\boldsymbol{w}(\boldsymbol{\mu}))} \qquad (5.10)$$

where c, d, A and E are constants and $(c - \boldsymbol{w}(\boldsymbol{\mu}))$ represents the oxidizer concentration. Dirichlet boundary condition is prescribed at the inlet:

$$\boldsymbol{w}(0, y; \boldsymbol{\mu}) = 0 \qquad y \in [0, H_o)$$

$$\boldsymbol{w}(0, y; \boldsymbol{\mu}) = c \qquad y \in [H_o, H_o + H_f]$$

$$\boldsymbol{w}(0, y; \boldsymbol{\mu}) = 0 \qquad y \in (H_o + H_f, H]$$

whereas homogeneous Neumann boundary conditions are prescribed on other boundaries.
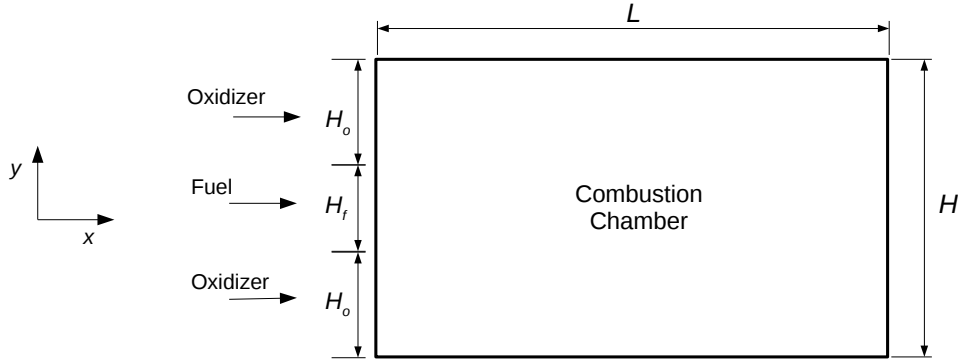
Figure 5.14: Schematic of the combustion chamber

In this problem, we consider parameter variations in three dimensions where $\boldsymbol{\mu} = [W_y, ln(A), r]$ consists of the velocity field in y-direction W_y, Arrhenius parameter $ln(A)$ and ratio of fuel to oxidizer inlet widths $r = H_f/H_o$. W_y, $ln(A)$ and r influence the direction, length and width of the flame, respectively. The values of the remaining constants are: $\boldsymbol{W}_x = 0.17\text{m/s}$, $\nu = 5 \times 10^{-6}\text{m}^2/\text{s}$, $c = 0.2$, $d = 0.24$ and $E = 0.1091$. The equations are discretized in space using a second-order, central finite difference scheme on a uniform Cartesian grid which is divided into 1 million grid points with $\Delta x = \Delta y = 10^{-5}\text{mm}$. A fine discretization is chosen to demonstrate the speedup associated with the hyper-reduction approach. The resulting equations are solved using Newton's method until convergence of 10 orders of magnitude. Fig. 5.15 shows the fuel concentration contours computed at eight different corners of the 3-D parameter space. Clear and distinct flame fronts having different directions, lengths and widths can be observed in these plots.

(a) Contour plot at $\boldsymbol{\mu} = [-0.02, 7.0, 0.467]$

(b) Contour plot at $\boldsymbol{\mu} = [-0.02, 7.0, 1.364]$

(c) Contour plot at $\boldsymbol{\mu} = [-0.02, 7.6, 0.467]$

(d) Contour plot at $\boldsymbol{\mu} = [-0.02, 7.6, 1.364]$

(e) Contour plot at $\boldsymbol{\mu} = [0.04, 7.0, 0.467]$

(f) Contour plot at $\boldsymbol{\mu} = [0.04, 7.0, 1.364]$

(g) Contour plot at $\boldsymbol{\mu} = [0.04, 7.6, 0.467]$

(h) Contour plot at $\boldsymbol{\mu} = [0.04, 7.6, 1.364]$

Figure 5.15: Fuel concentration $\boldsymbol{w}(\boldsymbol{\mu})$ contours computed at eight different corners of the 3-D parameter space $\mathcal{D}$

5.3.2   Implementation of TSMOR

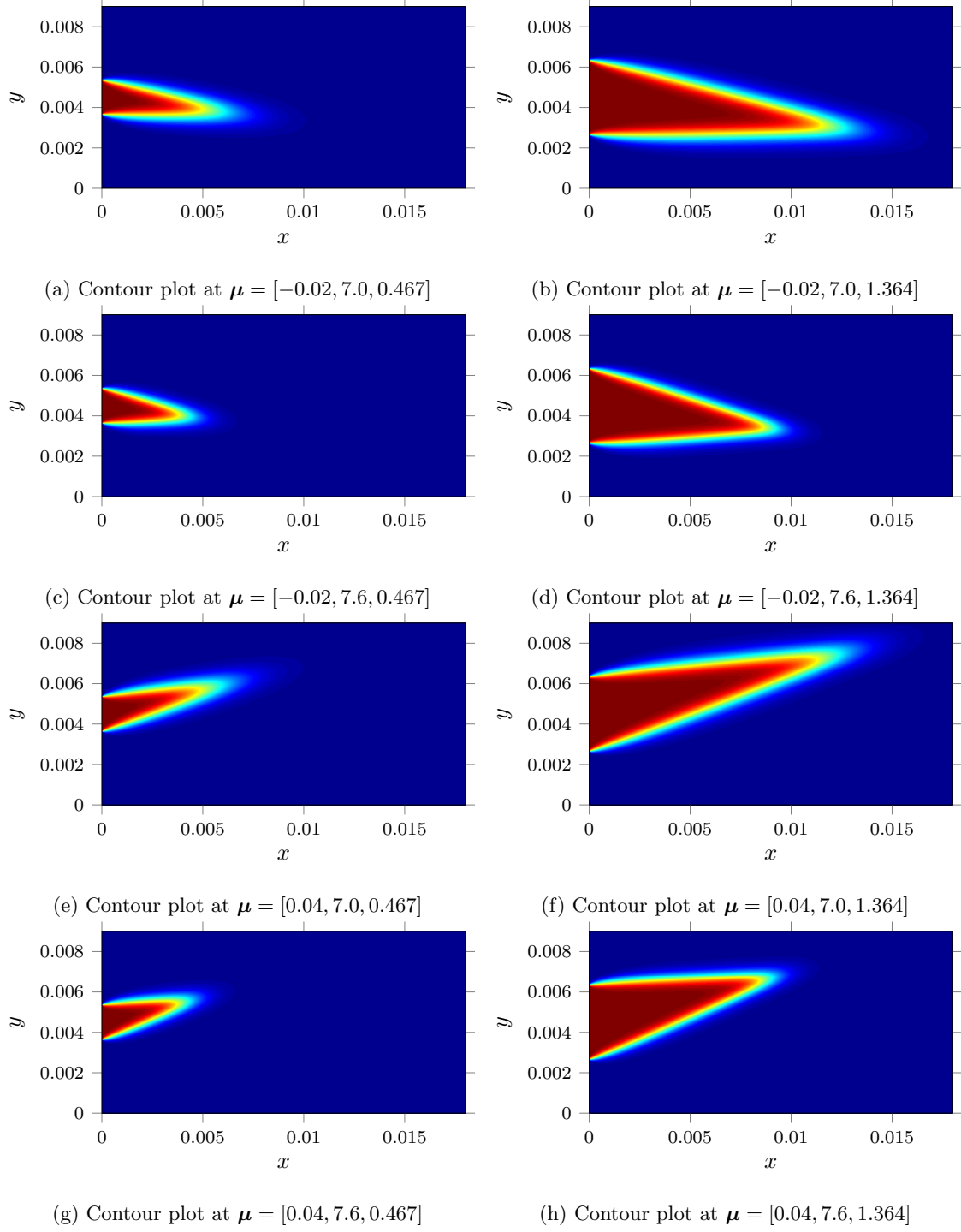A snapshot matrix $\boldsymbol{M}$ containing 48 snapshots is generated on a $4 \times 4 \times 3$ grid in parameter space $\mathcal{D}$ at parameters $W_y \times ln(A) \times r \equiv [-0.02, 0, 0.02, 0.04] \times [7.0, 7.2, 7.4, 7.6] \times [0.467, 0.846, 1.364]$.

Transport matrices for each snapshot $\boldsymbol{\Psi}(\boldsymbol{\mu}_s)$ are computed offline by solving the training error minimization (3.10). Since parameter W_y changes the angle of the flame, a strong coupling between x and y coordinates is required. As a result, the transport matrices are expressed as a coupled Fourier sine series with 11 modes each:

$$\boldsymbol{\Psi}_x(\boldsymbol{\mu}_s)_{(:,j)} = c_{x_0}^{s(j)} \sin\left(\frac{\pi\boldsymbol{x}}{2L}\right) + \sum_{p=1}^{p=3}\left[c_{x_p}^{s(j)} \sin\left(\frac{p\pi\boldsymbol{x}}{L}\right) + c_{x_{p+3}}^{s(j)} \sin\left(\frac{p\pi\boldsymbol{y}}{H}\right)\right] + \sum_{p,q=1}^{p,q=2} c_{x_t}^{s(j)} \sin\left(\frac{p\pi\boldsymbol{x}}{L}\right) \sin\left(\frac{q\pi\boldsymbol{y}}{H}\right)$$

$$\boldsymbol{\Psi}_y(\boldsymbol{\mu}_s)_{(:,j)} = c_{y_0}^{s(j)} \sin\left(\frac{\pi\boldsymbol{x}}{2L}\right) + \sum_{p=1}^{p=3}\left[c_{y_p}^{s(j)} \sin\left(\frac{p\pi\boldsymbol{x}}{L}\right) + c_{y_{p+3}}^{s(j)} \sin\left(\frac{p\pi\boldsymbol{y}}{H}\right)\right] + \sum_{p,q=1}^{p,q=2} c_{y_t}^{s(j)} \sin\left(\frac{p\pi\boldsymbol{x}}{L}\right) \sin\left(\frac{q\pi\boldsymbol{y}}{H}\right)$$

$$(5.11)$$

where $t = 7, \ldots, 10$. Transport of the boundary nodes can be controlled by fixing selected Fourier coefficients. For instance, from Fig. 5.15 it can be seen that the x-coordinates at the inlet are stationary, hence they need not be transformed while computing the transported snapshots. This boundary condition is enforced on the transport matrix $\boldsymbol{\Psi}_x(\boldsymbol{x}=0, \boldsymbol{y}; \boldsymbol{\mu}_s)_{(:,j)} = 0$ by fixing $c_{x_p}^{s(j)} = 0$ for $p = 4, 5, 6$. For this multi-dimensional parameter problem, $\boldsymbol{d}(\boldsymbol{\Delta\mu})$ is given by:

$$\boldsymbol{d}(\boldsymbol{\Delta\mu}) = \begin{bmatrix} \Delta\mu_1 \\ \Delta\mu_2 \\ \Delta\mu_3 \\ \Delta\mu_1\Delta\mu_2 \\ \Delta\mu_2\Delta\mu_3 \\ \Delta\mu_3\Delta\mu_1 \\ \Delta\mu_1\Delta\mu_2\Delta\mu_3 \end{bmatrix} \tag{5.12}$$

Transformation of structured Cartesian x and y coordinates based on the transports (5.11) leads to a non-tensor grid. Hence, interpolation from the non-tensor transported grid to the Eulerian grid must be performed using the `scatteredInterpolant` algorithm in Matlab. Unfortunately, this interpolation scheme is computational prohibitive for large grids. Therefore, during the precomputation stage, the snapshots are uniformly downsampled by a factor of 25 in x and y coordinates. This yields a coarse computational grid with approximately 2700 grid points.

Next, the TSMOR approach is equipped with the hyper-reduction strategy mentioned in Sec. 4.2. First,

70 collocation points are obtained by employing the DEIM algorithm. Second, these points are augmented with 30 uniformly distributed inlet points. Finally, an additional $\hat{n}_w \approx n_w \times 4 = 400$ points $\hat{\varepsilon}$ are included to enable the evaluation of the residuals via the central finite difference scheme.

$\boldsymbol{\mu}^*$	$\boldsymbol{\mu}_1^* \equiv W_y$	$\boldsymbol{\mu}_2^* \equiv ln(A)$	$\boldsymbol{\mu}_3^* \equiv r$
Case 1	-0.01	7.1	0.643
Case 2	0.005	7.3	1.083
Case 3	0.015	7.35	0.643
Case 4	0.025	7.5	1.083

Table 5.1: Table of four predictive test cases

To demonstrate the performance of the proposed TSMOR approach, solutions are predicted at four different predictive regimes in the parameter space $\mathcal{D}$ and compared with FOM and several other MOR techniques. Parameters corresponding to these test cases are tabulated in Table. 5.1. Figs. 5.16- 5.19 illustrate the predictive capabilities of several MOR approaches for these test cases. Contour plots at contour levels $\boldsymbol{w}(\boldsymbol{\mu}^*) = 0.018$ and $\boldsymbol{w}(\boldsymbol{\mu}^*) = 0.15$ are displayed in these figures. The FOM is given by the gray lines while the new proposed hyper-reduced TSMOR approach using 8 local basis is given by the red lines. The blue lines correspond to the solution obtained by LSPG using 48 POD modes of the snapshot matrix $\boldsymbol{M}$. The green lines correspond to L_1-dictionary approach using 8 local basis or dictionary elements. The proposed TSMOR approach predicts a solution which accurately matches the FOM solutions in all the four cases. In contrast, both LSPG and L_1-dictionary methods fail to capture the flame-front.

The ROM errors for the various MOR approaches considered are summarized in Table 5.2. Solutions predicted using TSMOR have an average error of only 2% as compared to 28% in LSPG and 17% in the L_1-dictionary approach. The table also provides the error in the POD-projected solution which is obtained by projecting the FOM onto 48 POD basis of the snapshot matrix $\boldsymbol{M}$. The average error for the POD-projected solution is 8.7%. Thus, TSMOR significantly outperforms LSPG and L_1-dictionary approaches and it is 3-4 times better than POD-projected solutions.

Finally, wall-times and speed-ups for the FOM and online stage of hyper-reduced TSMOR are given in Table. 5.3. TSMOR+HR delivers a speed-up of approximately between 150-300.
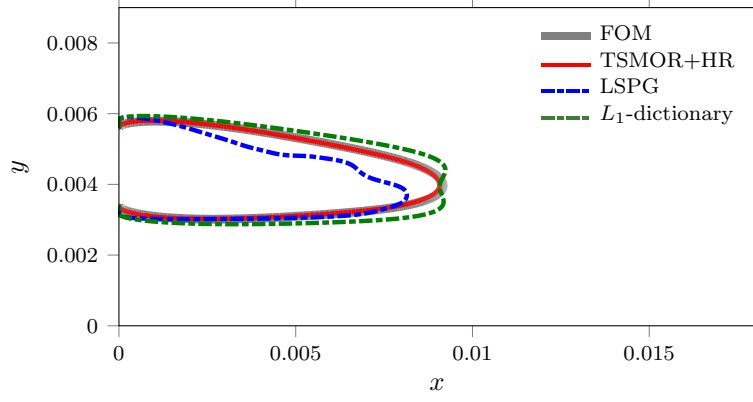
(a) Contour plot for $\boldsymbol{w}(\boldsymbol{\mu}^*) = 0.018$
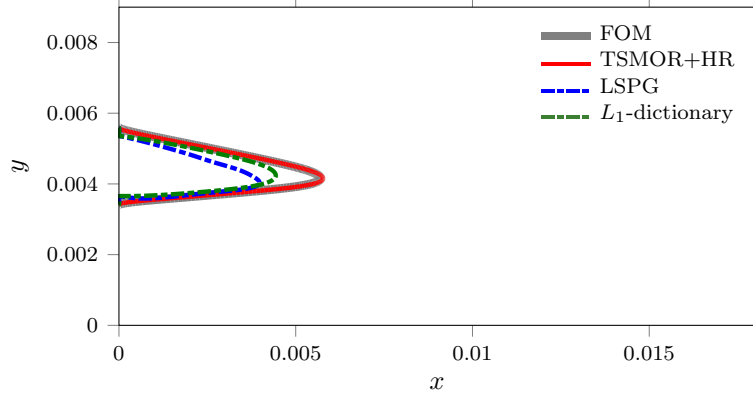
(b) Contour plot for $\boldsymbol{w}(\boldsymbol{\mu}^*) = 0.15$

Figure 5.16: Case 1: Comparison of predicted solution at $\boldsymbol{\mu^*} = [-0.01, 7.1, 0.644]$ using hyper-reduced TSMOR, LSPG and L_1-dictionary approach with FOM

Model	TSMOR+HR (8 local basis)	POD-Projection (48 global basis)	LSPG (48 global basis)	L_1-dictionary (8 local basis)
Case 1	1.07	9.12	27.34	15.49
Case 2	2.47	8.43	23.95	18.54
Case 3	1.24	8.72	32.74	18.25
Case 4	2.92	8.32	32.07	17.83

Table 5.2: Comparison of relative error (%) in the predicted solution at $\boldsymbol{\mu}^*$ for four different cases
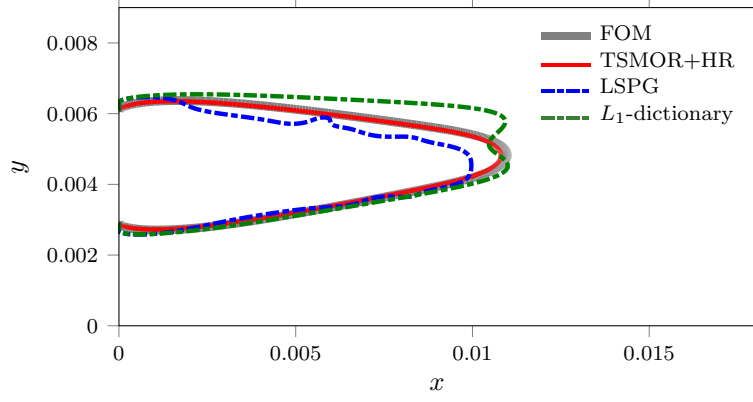
(a) Contour plot for $\boldsymbol{w}(\boldsymbol{\mu}^*) = 0.018$

(b) Contour plot for $\boldsymbol{w}(\boldsymbol{\mu}^*) = 0.15$

Figure 5.17: Case 2: Comparison of predicted solution at $\boldsymbol{\mu}^* = [0.005, 7.3, 1.083]$ using hyper-reduced TSMOR, LSPG and L_1-dictionary approach with FOM

Model	FOM	TSMOR+HR	Speed-up
Case 1	150 s	0.43 s	348
Case 2	150 s	0.67 s	223
Case 3	150 s	0.62 s	242
Case 4	150 s	0.94 s	160

Table 5.3: Comparison of wall-times and speed-ups associated with the FOM and online stage of hyper-reduced TSMOR for the prediction at $\boldsymbol{\mu}^*$ for four different cases

(a) Contour plot for $\boldsymbol{w}(\boldsymbol{\mu}^*) = 0.018$

(b) Contour plot for $\boldsymbol{w}(\boldsymbol{\mu}^*) = 0.15$

Figure 5.18: Case 3: Comparison of predicted solution at $\boldsymbol{\mu}^* = [0.015, 7.35, 0.644]$ using hyper-reduced TSMOR, LSPG and L_1-dictionary approach with FOM
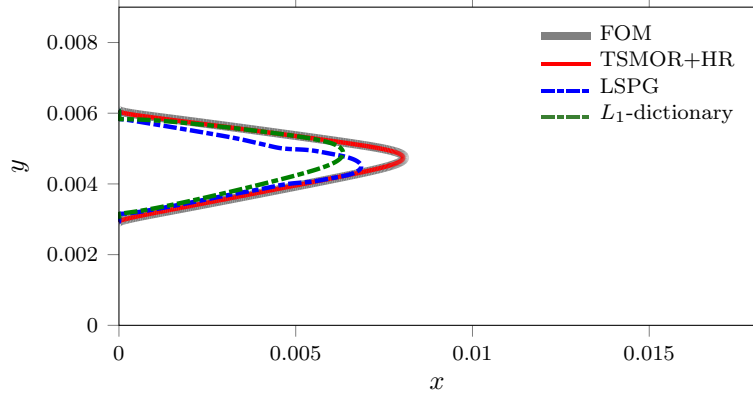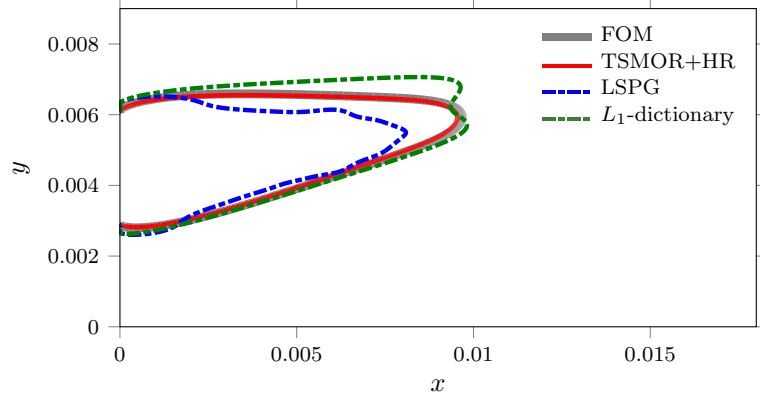
(a) Contour plot for $\boldsymbol{w}(\boldsymbol{\mu}^*) = 0.018$
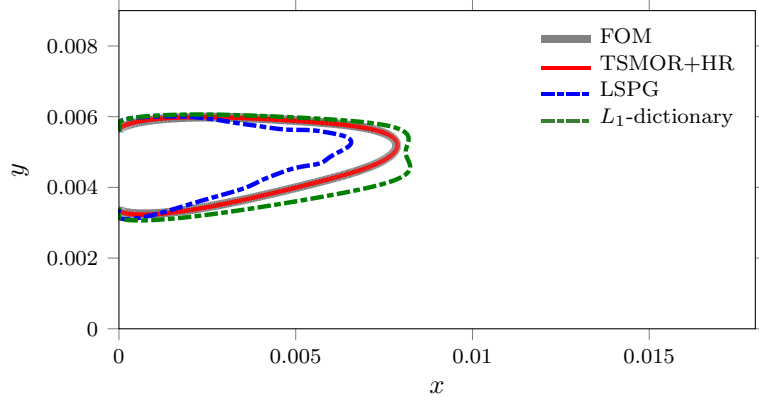

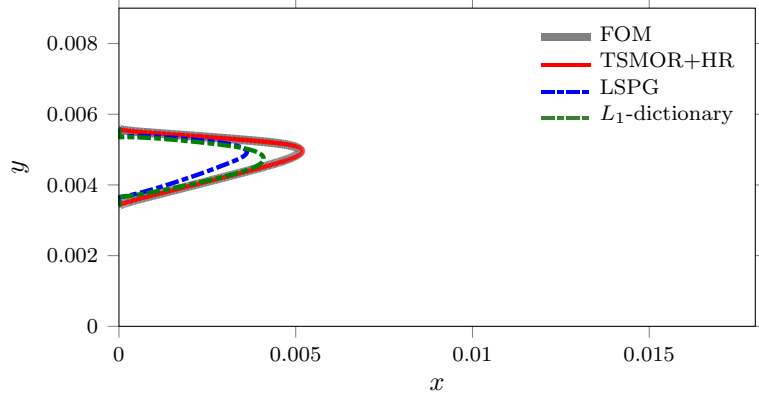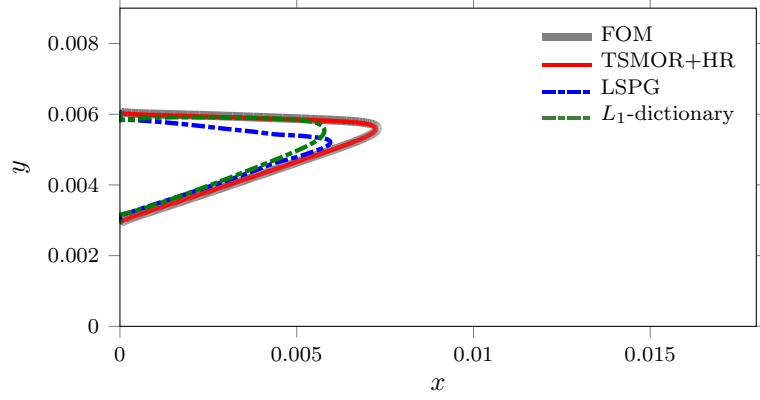(b) Contour plot for $\boldsymbol{w}(\boldsymbol{\mu}^*) = 0.15$

Figure 5.19: Case 4: Comparison of predicted solution at $\boldsymbol{\mu}^* = [0.025, 7.5, 1.083]$ using hyper-reduced TSMOR, LSPG and L_1-dictionary approach with FOM

Chapter 6

Conclusions and future work

In this thesis, a transported snapshot model order reduction (TSMOR) method for predicting new parametrical steady state solutions containing moving shocks and discontinuities is presented. In this method, the solution is approximated by a linear combination of spatially transported snapshots. The transports are assumed to be smooth in parameter as well as physical space, and hence approximated as a low-order polynomial expansion in both these variables. The coefficients of the polynomial expansion are obtained by training the data in the precomputation stage. The generalized coordinates are derived by solving a residual minimization problem in the online stage. TSMOR is also integrated with hyper-reduction methods to reduce the computational complexity. Numerical experiments consist of a 1-D converging-diverging nozzle problem with throat area as the parameter, supersonic flow over a forward facing step with inlet Mach number as the parameter and multi-dimensional parametric combustion problem with three parameters influencing the length, direction and width of the diffusion flame. For all parameters considered, TSMOR is demonstrated to significantly outperform traditional approaches such as those based on linear compression schemes e.g. LSPG and more recent local basis approaches such as L_1-dictionary. Furthermore, speed-up of two and four orders of magnitude for the combustion and nozzle problems are achieved, respectively.

The proposed approach is open to multiple extensions for future work. Firstly, TSMOR performance could be improved by incorporating more sophisticated hyper-reduction strategies such as GNAT, DEIM, or ECSW. Secondly, an adaptive greedy sampling [16] strategy could be employed to minimizes the prediction error based on error-estimates. Similar to most current parametric MOR approach, our proposed approach suffers from the curse of dimensionality for high-dimensional parameter variations. More sophisticated sampling strategies and alternate low-order expansions will therefore have to be explored. Finally, to validate the proposed approach further, more realistic three-dimensional and time-dependent high-fidelity models should be considered.

References

[1] B. Galletti, C.H. Bruneau, L. Zannetti, and A. Iollo. Low-order modelling of laminar flow regimes past a confined square cylinder. *Journal of Fluid Mechanics*, 503:161–170, 2004.

[2] P. Holmes, J.L. Lumley, G. Berkooz, and C.W. Rowley. *Turbulence, coherent structures, dynamical systems and symmetry*. 2nd ed., Cambridge University Press, 2012.

[3] C.W. Rowley, I. Mezić, S. Bagheri, P. Schlatter, and D.S. Henningson. Spectral analysis of nonlinear flows. *Journal of Fluid Mechanics*, 641:115–127, 2009.

[4] P.J. Schmid. Dynamic mode decomposition of numerical and experimental data. *Journal of Fluid Mechanics*, 656:5–28, 2010.

[5] G. Rozza. Reduced basis approximation and error bounds for potential flows in parametrized geometries. *Communications in Computational Physics*, 9(1):1–48, 2011.

[6] K. Veroy and A.T. Patera. Certified real-time solution of the parametrized steady incompressible Navier–Stokes equations: rigorous reduced-basis a posteriori error bounds. *International Journal for Numerical Methods in Fluids*, 47(8-9):773–788, 2005.

[7] S. Gugercin and A.C. Antoulas. A survey of model reduction by balanced truncation and some new results. *International Journal of Control*, 77(8):748–766, 2004.

[8] B. Moore. Principal component analysis in linear systems: Controllability, observability, and model reduction. *IEEE Transactions on Automatic Control*, 26(1):17–32, 1981.

[9] S. Lall, J. E. Marsden, and S. Glavaški. A subspace approach to balanced truncation for model reduction of nonlinear control systems. *International Journal of Robust and Nonlinear Control*, 12(6):519–535, 2002.

[10] P. Benner, J.R. Li, and T. Penzl. Numerical solution of large-scale Lyapunov equations, Riccati equations, and linear-quadratic optimal control problems. *Numerical Linear Algebra with Applications*, 15(9): 755–777, 2008.

[11] J.R. Li and J. White. Low rank solution of Lyapunov equations. *SIAM Journal on Matrix Analysis and Applications*, 24(1):260–280, 2002.

[12] C.W. Rowley. Model reduction for fluids, using balanced proper orthogonal decomposition. In *Modeling And Computations In Dynamical Systems: In Commemoration of the 100th Anniversary of the Birth of John von Neumann*, pages 301–317. World Scientific, 2006.

[13] K. Willcox and J. Peraire. Balanced model reduction via the proper orthogonal decomposition. *AIAA Journal*, 40(11):2323–2330, 2002.

[14] P. Benner, S. Gugercin, and K. Willcox. A survey of projection-based model reduction methods for parametric dynamical systems. *SIAM Review*, 57(4):483–531, 2015.

[15] R.L. Iman. *Latin hypercube sampling*. Wiley Online Library, 2008.

[16] A. Paul-Dubois-Taine and D. Amsallem. An adaptive and efficient greedy procedure for the optimal training of parametric reduced-order models. *International Journal for Numerical Methods in Engineering*, 102(5):1262–1292, 2015.

[17] G. Rozza, D.B.P. Huynh, and A.T. Patera. Reduced basis approximation and a posteriori error estimation for affinely parametrized elliptic coercive partial differential equations. *Archives of Computational Methods in Engineering*, 15(3):229, 2008.

[18] T. Bui-Thanh, K. Willcox, and O. Ghattas. Parametric reduced-order models for probabilistic analysis of unsteady aerodynamic applications. *AIAA Journal*, 46(10):2520, 2008.

[19] T. Bui-Thanh, K. Willcox, and O. Ghattas. Model reduction for large-scale systems with high-dimensional parametric input space. *SIAM Journal on Scientific Computing*, 30(6):3270–3288, 2008.

[20] M. Rewieński and J. White. Model order reduction for nonlinear dynamical systems based on trajectory piecewise-linear approximations. *Linear Algebra and its Applications*, 415(2-3):426–454, 2006.

[21] T. Lieu, C. Farhat, and M. Lesoinne. Reduced-order fluid/structure modeling of a complete aircraft configuration. *Computer Methods in Applied Mechanics and Engineering*, 195(41):5730–5742, 2006.

[22] D. Amsallem, J. Cortial, and C. Farhat. Toward real-time computational-fluid-dynamics-based aeroelastic computations using a database of reduced-order information. *AIAA Journal*, 48(9):2029–2037, 2010.

[23] K. Carlberg, C. Bou-Mosleh, and C. Farhat. Efficient non-linear model reduction via a least-squares Petrov–Galerkin projection and compressive tensor approximations. *International Journal for Numerical Methods in Engineering*, 86(2):155–181, 2011.

[24] M.J. Zahr, D. Amsallem, and C. Farhat. Construction of parametrically-robust CFD-based reduced-order models for PDE-constrained optimization. *AIAA Paper*, 2845:26–29, 2013.

[25] D. Amsallem, J. Cortial, K. Carlberg, and C. Farhat. A method for interpolating on manifolds structural dynamics reduced-order models. *International Journal for Numerical Methods in Engineering*, 80(9):1241–1258, 2009.

[26] M. Yano, A.T. Patera, and K. Urban. A space-time certified reduced basis method for Burgers' equation. *Mathematical Models and Methods in Applied Sciences*, 24(09):1903–1935, 2014.

[27] W. Dahmen. How to best sample a solution manifold? In *Sampling Theory, a Renaissance*, pages 403–435. Springer, 2015.

[28] D. Amsallem and C. Farhat. An online method for interpolating linear parametric reduced-order models. *SIAM Journal on Scientific Computing*, 33(5):2169–2198, 2011.

[29] T. Bui-Thanh, M. Damodaran, and K. Willcox. Proper orthogonal decomposition extensions for parametric applications in compressible aerodynamics. *AIAA Paper*, 4213, 2003.

[30] K. Washabaugh, D. Amsallem, M. Zahr, and C. Farhat. Nonlinear model reduction for CFD problems using local reduced-order bases. In *42nd AIAA Fluid Dynamics Conference and Exhibit, Fluid Dynamics and Co-located Conferences, AIAA Paper*, volume 2686, pages 1–16, 2012.

[31] D. Amsallem, M.J. Zahr, and C. Farhat. Nonlinear model order reduction based on local reduced-order bases. *International Journal for Numerical Methods in Engineering*, 92(10):891–916, 2012.

[32] T. Franz, R. Zimmermann, S. Görtz, and N. Karcher. Interpolation-based reduced-order modelling for steady transonic flows via manifold learning. *International Journal of Computational Fluid Dynamics*, 28(3-4):106–121, 2014.

[33] T. Hummel, C. Temmler, B. Schuermans, and T. Sattelmayer. Reduced-order modeling of aeroacoustic systems for stability analyses of thermoacoustically noncompact gas turbine combustors. *Journal of Engineering for Gas Turbines and Power*, 138(5):051502, 2016.

[34] M. Balajewicz and C. Farhat. Reduction of nonlinear embedded boundary models for problems with evolving interfaces. *Journal of Computational Physics*, 274:489–504, 2014.

[35] M. Balajewicz and J. Toivanen. Reduced order models for pricing American options under stochastic volatility and jump-diffusion models. *Procedia Computer Science*, 80:734–743, 2016.

[36] K. Washabaugh, M.J. Zahr, and C. Farhat. On the use of discrete nonlinear reduced-order models for the prediction of steady-state flows past parametrically deformed complex geometries. In *54th AIAA Aerospace Sciences Meeting*, page 1814, 2016.

[37] D. Rim, S. Moe, and R.J. LeVeque. Transport reversal for model reduction of hyperbolic partial differential equations. *arXiv preprint arXiv:1701.07529*, 2017.

[38] S. Mowlavi and T.P. Sapsis. Model order reduction for stochastic dynamical systems with continuous symmetries. *arXiv preprint arXiv:1704.06352*, 2017.

[39] C.W. Rowley and J.E. Marsden. Reconstruction equations and the Karhunen–Loève expansion for systems with symmetry. *Physica D: Nonlinear Phenomena*, 142(1):1–19, 2000.

[40] A. Iollo and D. Lombardi. Advection modes by optimal mass transfer. *Physical Review E*, 89(2):022923, 2014.

[41] R. Abgrall, D. Amsallem, and R. Crisovan. Robust model reduction by L^1-norm minimization and approximation via dictionaries: application to nonlinear hyperbolic problems. *Advanced Modeling and Simulation in Engineering Sciences*, 3(1):1, 2016.

[42] K. Carlberg. Adaptive h-refinement for reduced-order models. *International Journal for Numerical Methods in Engineering*, 102(5):1192–1210, 2015.

[43] M. Ohlberger and S. Rave. Nonlinear reduced basis approximation of parameterized evolution equations via the method of freezing. *Comptes Rendus Mathematique*, 351(23):901–906, 2013.

[44] R. Mojgani and M. Balajewicz. Lagrangian basis method for dimensionality reduction of convection dominated nonlinear flows. *arXiv preprint arXiv:1701.04343*, 2017.

[45] D.J. Lucia, P.I. King, M.E. Oxley, and P.S. Beran. Reduced order modeling for a one-dimensional nozzle flow with moving shocks. *AIAA Paper*, 2602:2001, 2001.

[46] P.G. Constantine and G. Iaccarino. Reduced order models for parameterized hyperbolic conservations laws with shock reconstruction. *Center for Turbulence Research Annual Brief*, 2012.

[47] N. Cagniart, R. Crisovan, Y. Maday, and R. Abgrall. Model order reduction for hyperbolic problems: a new framework. 2017.

[48] J. Reiss, P. Schulze, J. Sesterhenn, and V. Mehrmann. The shifted proper orthogonal decomposition: A mode decomposition for multiple transport phenomena. *arXiv preprint arXiv:1512.01985*, 2015.

[49] G. Welper. Interpolation of functions with parameter dependent jumps by transformed snapshots. *SIAM Journal on Scientific Computing*, 39(4):A1225–A1250, 2017.

[50] P.W. Holland and R.E. Welsch. Robust regression using iteratively reweighted least-squares. *Communications in Statistics-theory and Methods*, 6(9):813–827, 1977.

[51] I. Daubechies, R. DeVore, M. Fornasier, and C.S. Güntürk. Iteratively reweighted least squares minimization for sparse recovery. *Communications on Pure and Applied Mathematics*, 63(1):1–38, 2010.

[52] S. Chaturantabut and D.C. Sorensen. Nonlinear model reduction via discrete empirical interpolation. *SIAM Journal on Scientific Computing*, 32(5):2737–2764, 2010.

[53] K. Carlberg, J. Cortial, D. Amsallem, M. Zahr, and C. Farhat. The GNAT nonlinear model reduction method and its application to fluid dynamics problems. In *6th AIAA Theoretical Fluid Mechanics Conference*, volume 2730, pages 2011–3112, 2011.

[54] C. Farhat, P. Avery, T. Chapman, and J. Cortial. Dimensional reduction of nonlinear finite element dynamic models with finite rotations and energy-based mesh sampling and weighting for computational efficiency. *International Journal for Numerical Methods in Engineering*, 98(9):625–662, 2014.

[55] K. Carlberg, C. Farhat, J. Cortial, and D. Amsallem. The GNAT method for nonlinear model reduction: effective implementation and application to computational fluid dynamics and turbulent flows. *Journal of Computational Physics*, 242:623–647, 2013.

[56] G. Welper. *h* and *hp*-adaptive interpolation by transformed snapshots for parametric and stochastic hyperbolic PDEs. *arXiv preprint arXiv:1710.11481*, 2017.

[57] D. Galbally, K. Fidkowski, K. Willcox, and O. Ghattas. Non-linear model reduction for uncertainty quantification in large-scale inverse problems. *International Journal for Numerical Methods in Engineering*, 81(12):1581–1608, 2010.

[58] P. Woodward and P. Colella. The numerical simulation of two-dimensional fluid flow with strong shocks. *Journal of Computational Physics*, 54(1):115–173, 1984.

[59] S. Gottlieb. On high order strong stability preserving Runge–Kutta and multi step time discretizations. *Journal of Scientific Computing*, 25(1):105–128, 2005.